DIPLOMARBEIT

Characterisation of the Polarised White Neutron Beam at the TRIGA Reactor of the Atominstitut

zur Erlangung des akademischen Grades

Diplom-Ingenieur

ausgeführt am Atominstitut
der Technischen Universität Wien

unter der Anleitung von
Em.Univ.Prof. Dipl.-Ing. Dr.techn. Gerald Badurek
und
Ass.Prof. Dipl.-Ing. Dr.techn. Erwin Jericha

durch

Christopher Philipp Burger-Scheidlin, BSc
Matr. Nr. 01227388

Wien, 11. Februar 2019

(Unterschrift Verfasser) (Unterschrift Betreuer)

Abstract

In 1963 G. M. Drabkin introduced the idea of constructing a neutron resonator capable of monochromatising a white polarised neutron beam through the magnetic interaction of the spins. Nearly 30 years later, G. Badurek *et al.* published the proposition of improving the original setup by splitting the resonator into separately controllable coils improving the resolution of the device.

The Monopol group at the Atominstitut (ATI) of the TU Wien was formed. It constructed such a 'Badurek-type' resonator and performed experiments with dichromatic thermal neutrons as well as very cold neutrons. Henceforth, the resonator should be used for a Maxwell-Boltzmann-distributed white thermal neutron beam. The aim of this thesis was to establish initial measurements at the 'Thermal White Neutron Beam Facility' (TWB) of the ATI showing the possibilities of polarised neutron experiments with such a beam by imitating the Monopol 4.0 resonator with very basic components and improving the understanding of them. The resonator itself will soon be ready for use. Through experiments at the TWB the characteristics of the group's neutron supermirrors including the possible degree of polarisation as well as the efficiencies of spin-manipulating devices, such as a current-sheet and DC-coil flippers, could be evaluated. Close to 350 time-of-flight measurements gave an insight into the spectral distribution and provided means to show wavelength-dependent effects when rotating the polarisers in the beam, applying different magnetic field strengths to the spin flippers and a guiding field. The results of this work have shown that it is possible to successfully polarise and manipulate the thermal white beam with the available hardware. It could be shown in what way the spin flip devices altered the time-of-flight spectra and where the limits of the present hardware lie.

In addition, work directly dedicated to the resonator, such as testing of electronics, assembly and careful examination of bodies for the power components had to be done, as well as simulations for a current-smoothing setup of a high-performance power supply.

Zusammenfassung

1963 stellte G. M. Drabkin die Idee eines Neutronenresonators vor, der durch magnetische Interaktion mit den Neutronenspins die Fähigkeit haben sollte, einen weißen, polarisierten Neutronenstrahl zu monochromatisieren. Fast 30 Jahre später publizierten G. Badurek *et. al.* den Vorschlag, die Auflösung des Experiments zu verbessern und den originalen Aufbau durch separat ansteuerbare Spulen zu modifizieren.

Die Monopol - Gruppe am Atominstitut (ATI) der Technischen Universität Wien wurde 2010 gegründet. Sie konstruierte solch einen 'Badurek-Typ' Resonator und führte Experimente mit dichromatischen, thermischen Neutronen und sehr kalten Neutronen durch. Weiterführend sollte der Resonator an einem Maxwell-Boltzmann-verteilten, weißen thermischen Neutronenstrahl eingesetzt werden.

Das Ziel der vorliegenden Arbeit war die Durchführung erster Messungen am thermischen weißen Neutronenstrahlplatz (TWB) des ATI, um die Möglichkeiten von Experimenten mit polarisierten Neutronen an dem neuen Strahlplatz aufzuzeigen. Der Resonator Monopol 4.0, der bald in voller Funktionalität zu Verfügung stehen wird, sollte mit sehr vereinfachten Komponenten imitiert werden, um die einzelnen Elemente des Aufbaus besser zu verstehen. Durch Experimente am TWB konnten die Charakteristiken der Neutronen-Superspiegel der Arbeitsgruppe wie deren möglicher Polarisationsgrad sowie die Effizienzen der spinmanipulierenden Komponenten wie die eines Stromblatts und zweier Gleichstrom-Spindreher berechnet werden. Fast 350 Flugzeitmessungen gewährten einen Einblick dahingehend, wie sich die spektrale Verteilung änderte und stellten Mittel bereit, um wellenlängenabhängige Effekte bei der Rotation der Polarisatoren im Neutronenstrahl und beim Anlegen verschiedener Magnetfeldstärken an den Spindrehern und an dem Führungsfeld aufzuzeigen.

Die Ergebnisse lassen darauf schließen, dass es möglich ist, eine Polarisation und Manipulation des weißen Strahls mit den vorhandenen Instrumenten zu erwirken. Es konnte außerdem gezeigt werden, inwiefern das verwendete Stromblatt und die Spindreher die Spektren der Flugzeitmessungen verändern und wo die Grenzen des derzeitigen Aufbaus liegen.

Zusätzlich wurden Arbeiten direkt für den Resonator selbst verrichtet. Dazu gehörte etwa das Testen der Elektronik sowie der Zusammenbau samt sorgfältiger Überprüfung der Kühlkörper für die Leistungselektronik, aber auch Simulationen einer Glättungsschaltung für eine Hochleistungsstromversorgung.

Contents

Glossary of Symbols

Glossary of Symbols

Å	$=10^{-10}$ m, Ångström
a	Length of an object
B	Magnetic field strength
B_0	Magnetic guiding field strength
B_1	Magnetic alternating field strength
$\vec{B}_\omega$	Magnetic field strength vector with respective origin ω
$\|B\|$	Absolute value of the magnetic field strength
B_x, B_y, B_z	Magnetic field strength in the respective direction
b	$=10^{-28}$ m^2, barn
β	Ratio of the alternating magnetic field over the selector field multiplied with a constant
$C(t)$	Chopper opening function
c	Velocity of light
d	Length of an object
d_{hkl}	Interplanar spacing between the (hkl) planes in a crystalline solid
E	Kinetic energy of a neutron
$\overline{E}$	Mean kinetic energy of an ensemble of neutrons
e_i	Efficiency of a device i
e	Elementary charge
e$^-$	Electron
eV	Electron volts, $1\,\mathrm{eV} = 1.602\,176\,620\,8(98) \times 10^{-19}$ J [1]
g	$=-3.826\,085\,45(90)$ T [1], neutron g-factor

γ	$=-1.832\,471\,72(34)\times10^{8}\,\mathrm{rad\,s^{-1}\,T}$ [1], neutron gyromagnetic ratio
h	$=6.626\,070\,040(81)\times10^{-34}\,\mathrm{J\,s}$ [1], Planck's constant
$\hbar$	$=1.054\,571\,800(13)\times10^{-34}\,\mathrm{J\,s}$ [1], Planck's constant devided by 2π, also known as Planck's reduced constant
k	$\in\mathbb{N}_0$, parameter
k_B	$=1.380\,648\,52(79)\times10^{-23}\,\mathrm{J\,K^{-1}}$ [1], Boltzmann's constant
L	Length of an object
λ	De Broglie wavelength of a neutron
λ_c	Critical wavelength
$\Delta\lambda$	Smallest difference in wavelengths that can be distinguished at a wavelength λ
$\bar{\lambda}$	Mean wavelength of an ensemble of neutrons
λ_0	Resonance wavelength
m	$=1.674\,927\,471(21)\times10^{-27}\,\mathrm{kg}$ [1], neutron mass; or ’m-value’, a measure of the reflectivity of a supermirror
m_p	$=1.672\,621\,898(21)\times10^{-27}\,\mathrm{kg}$ [1], proton mass
μ	$=-0.966\,236\,50(23)\times10^{-26}\,\mathrm{J\,T^{-1}}$ [1], magnetic momentum of the neutron
μ_N	$=5.050\,783\,699(31)\times10^{-27}\,\mathrm{J\,T^{-1}}$ [1], nuclear magneton
N	Number of spacial magnetic field periods; or neutron counts
N_{ij}	Number of transmitted neutrons with i and j representing the respective on (1) or off (0) state of a device
N_meas	Number of transmitted neutrons of a measurement
N_ref	Number of transmitted neutrons of the reference measurement
$N_\uparrow, N_\downarrow$	Number of transmitted spin neutrons in the respective ($\uparrow$) or ($\downarrow$) state
n	Order of reflection; or count rate
n^0	Neutron
$\bar{\nu}_\mathrm{e}$	Antineutrino
ω_L	Larmor frequency of a neutron
$\omega(\lambda)$	Wavelength-dependant rotation frequency
P	Polarising efficiency of a neutron polariser

$P_P P_A$	Degree of polarisation represented by the multiplication of the degree of polarisation of P_P and P_A
p	Neutron momentum
p^+	Proton
R	Radius
R_ω	Resistance of respective component ω
T	Neutron temperature in absolute units
t	Time
Δt	Chopper timing offset
τ	Dead time of a detector
ϑ	Polariser angle in respect to the neutron beam direction
$\bar{\theta}_b$	Bragg angle of reflection
θ_c	Critical angle of reflection
v	Neutron velocity
$\bar{v}$	Mean velocity of an ensemble of neutrons
$W(\lambda)$	Spin flip probability
Δy	Deviation from the parallel position in respect to the neutron beam direction

1 Introduction

In 1963 G. M. Drabkin [2] introduced the idea of constructing a neutron resonator, and in the following years developed the concept of spacial spin resonance much further. Four years after the first paper, the first resonator was built and its properties measured [3].
In 1991, G. Badurek *et al.* [4] mentioned the idea of improving the device by splitting the Drabkin resonator into many independent coils. In 2003, G. Badurek and E. Jericha [5] published the concepts to an advanced Drabkin resonator with its possible realisation of a travelling wave mode.
This lead to the forming of a new work group as the Monopol project. With funding from the Austrian FWF and the European Union, the first PhD-student, C. Gösselsberger [6], was put to the task of building such a device capable of tailoring the neutron beam suited to the requirements of the neutron beta-decay experiment Perc. The Proton Electron Radiation Channel is a large-scale experiment at FRM II in Garching, Germany. Consisting of a large evacuated decay volume for neutrons, large magnetic field coil around said volume are positioned to guide the charged decay products out of the neutron beam and into detectors. The goal of the experiment is to gain information on the weak force from the analysed decay products. It is in need of a well-prepared neutron beam that the Monopol resonator could provide.
To meet these requirements, the Monopol beam should have a cross section of 6 cm × 6 cm, a wavelength resolution $\Delta\lambda/\lambda \leq 0.1$ at 5 Å, a high degree of polarisation, a maximal transmitting intensity and a precisely defined time structure [6, p.64].
The first resonator prototype, Monopol 1.0 was built in 2010 at the Atominstitut (ATI) consisting of 10 individual coils. The initial experiments conducted were on a dichomatic beamline at the TRIGA reactor in Vienna.
Two years later, the prototype 2.0 consisting of 48 stages and upgraded components was constructed [7], [8].
During prototype 3.0, a prephase for the next resonator generation, upgrades to the

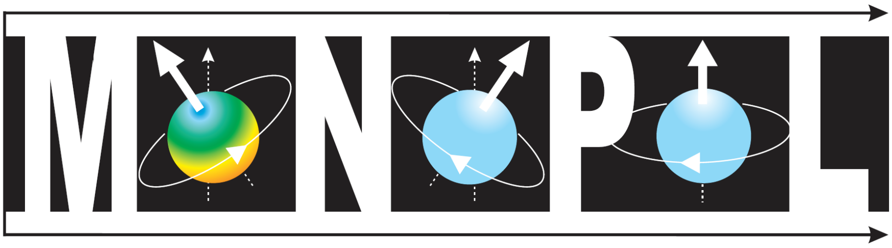

FIG. 1.1 – Logo of the MONOPOL project.

communications system were performed and a web interface was installed in the process. The next prototype, MONOPOL 3.1, received improved stages because of absorption problems. This version was successfully tested at the ILL in Grenoble, France for the first time in 2013 for very cold neutrons [9], [10], [11].
The current version of the resonator, MONOPOL 4.0, is still under construction making further progress. An appropriate beam site at the TRIGA reactor in Vienna was constructed recently headed by W. Mach [12]. The programming of the controllers in the low-level programming language 'Assembler' to guarantee exact timing control has been completed by A. Frank [13] as well as the intermediary GUI for the control and calculation of values by M. Sajatovic [14]. The main user interface will be realised by M. Wess [15].

When completed, MONOPOL 4.0 will be able to monochromatise a thermal white beam by definition of the central wavelength and the wavelength distribution around it. This means that it will be possible to define the time structure of the neutron beam for PERC by providing neutron pulses of arbitrary lengths from a few microseconds up to a few milliseconds, as well as continuous operation.

2 Theory

2.1 Properties of the neutron

The neutron was discovered by J. Chadwick [16] in 1932 and is classified as a baryon with the mass $m = 1.674 \times 10^{-27}\,\mathrm{kg}$* [1]. Its net charge is zero but despite this, due to the fact that the neutron is made up of three sub-particles (one up and two down quarks according to the standard model of particle physics), it has magnetic momentum. This magnetic momentum is $\mu = -1.913\,\mu_{\mathrm{N}}$, with $\mu_{\mathrm{N}} = 5.051 \times 10^{-27}\,\mathrm{J\,T^{-1}}$ being the nuclear magneton† [17, p.1].

It has spin angular momentum of $\frac{1}{2}$ with a magnitude of $\pm\frac{1}{2}\hbar$ complying with the Fermi-Dirac statistics. Neutron beams can be prepared to be predominantly in either the up state $(+\frac{1}{2}\hbar)$ or the down state $(-\frac{1}{2}\hbar)$, henceforth represented by $(\uparrow)$ and $(\downarrow)$, respectively. This polarisability is one of the main reasons the MONOPOL experiment is possible. How the preparation can be put into practice will be discussed in *Section* 2.3 [17].

Neutrons are stable as particles in the nuclei of atoms. However, the mean lifetime of a free neutron is 880.3(11) s [18]. When a neutron decays, the β^+ process

$$\mathrm{n}^0 \;\Rightarrow\; \mathrm{p}^+ + \mathrm{e}^- + \bar{\nu}_{\mathrm{e}} + 0.78\,\mathrm{MeV} \tag{2.1}$$

takes place.

The energies of neutrons are usually given in units of electron volts (eV) where $1\,\mathrm{eV} = 1.602 \times 10^{-19}\,\mathrm{J}$. The kinetic energy E of the neutron in combination with the neutron mass m determines its velocity v with

$$v = \left(\frac{2E}{m}\right)^{\frac{1}{2}} \quad , \tag{2.2}$$

---

[*] More precise values for the neutron mass and any other constants mentioned in this work can be found in the *Glossary of Symbols.*

[†] $\mu_{\mathrm{N}} = \frac{e\,\hbar}{2m_{\mathrm{p}}}$

Tab. 2.1 – Neutron energies. The compilation refers to the following sources: K. H. Beckurts and K. Wirtz [20], J. Bryne [21], D. Filges and F. Goldenbaum [22], and W. G. Williams [17].

Name	Energy range
Fast neutrons	$> 0.5\,\mathrm{MeV}$
Epithermal neutrons (intermediate energy neutrons)	$1\,\mathrm{eV} - 0.5\,\mathrm{MeV}$
Slow neutrons	
Hot neutrons	$0.1 - 1\,\mathrm{eV}$
Thermal neutrons	$10 - 100\,\mathrm{meV}$
Cold neutrons	$0.1 - 10\,\mathrm{meV}$
Very cold neutrons (VCN)	$0.3 - 100\,\mu\mathrm{eV}$
Ultra cold neutrons (UCN)	$< 300\,\mathrm{neV}$

and the de Broglie wavelength λ with

$$\lambda = \frac{h}{p} = \frac{h}{(2\,E\,m)^{\frac{1}{2}}} \quad , \tag{2.3}$$

with h being Planck's constant ($h = 6.626 \times 10^{-34}\,\mathrm{J\,s}$) [17, pp.1-2].

In addition, according to the equipartition theorem, an ensemble of neutrons with a mean kinetic energy $\overline{E}$ can be described as a gas following a Maxwell-Boltzmann distribution with a certain temperature T.

$$\overline{E} = \frac{m\,\bar{v}^2}{2} = k_B\,T \tag{2.4}$$

Neutrons are subject to all four fundamental forces. They interact with the electromagnetic force via their magnetic dipole momentum. The interaction with the gravitational force can be constituted because of their finite mass. The strong nuclear force is present in the nucleus, of which neutrons are part of, and plays a major role in neutron scattering. The β-instability shows that neutrons are also subjected to the weak nuclear force [19].

2.2 Neutron sources

Since free neutrons have a limited lifetime, as mentioned before, the sources have to be reasonably close to the location where they are produced for experimental purposes. Neutrons can generally be obtained through three different processes: Nuclear reactions, nuclear fission, and spallation.

2.2.1 Nuclear reactions

The fact that, compared to other atoms, some neutrons are more loosely bound in some atomic nuclei like in that of ^{9}Be can be used to produce free neutrons. When combining ^{9}Be with alpha emitters such as Pu or Am, the nucleus gains enough energy through the collision to compensate the binding energy and induce a nuclear reaction. In an Am-Be mixture, a neutron flux of up to $10^{7}\,\mathrm{s}^{-1}\,\mathrm{cm}^{-2}$ can be reached [23].

2.2.2 Nuclear fission

Nuclear fission takes place in nuclear reactor cores. A free neutron is absorbed by an atom and the entire kinetic energy of the particle is transferred to the nucleus. In addition, the binding energy between the neutron and the nucleus excite the nucleus. For heavy elements, these events can cause a destabilisation of the nucleus inducing an oscillation due to the repulsive forces between protons. This can consequently lead to the breaking apart of the nucleus into two separate fractions, one larger and one smaller nucleus, along with free neutrons. The reason for the emission of these free neutrons is that heavier elements have a higher neutron to proton ratio than lighter elements in order to be stable. This means that, when the two separate, smaller nuclei form. However, compared to the original isotope, these require fewer neutrons in order to be stable. The remaining neutrons then decay or are set free. These free neutrons have high energies (for the ^{235}U reaction, kinetic energies of around 2 MeV per neutron occur [24]) and need to then be slowed down through a process called moderation. This takes place when neutrons collide inelastically with the moderator material, usually (heavy) water or graphite. Through multiple collisions, the neutrons lose a majority of their kinetic energy and slow down. They can then be described as thermal neutrons with $\overline{E} \simeq 25\,\mathrm{meV}$ and can again be absorbed by another fissile nucleus that, consequentially, may split again setting free more neutrons. The result is a nuclear chain reaction and a continuous source of neutrons that can then be used to produce electric energy, or in the case of neutron scientists, to experiment with neutrons. To keep the number of fission reactions constant control rods usually made of boron, gadolinium or cadmium, elements that are very effective at absorbing neutrons, can be inserted into the core to regulate the reaction.

The *TRIGA Mark II* reactor at the *Atominstitut* in Vienna (ATI) is one of these scientific research reactors used for continuous neutron experiments. It was constructed by *General Atomics* in 1962 and reaches a continuous thermal power of 250 kW. Each of the about 80 U-Zr-H fuel elements contains 38 g of fissile uranium. The moderation of fast free neutrons is achieved by the zirconium hydrate on the one hand, and water surrounding the fuel elements on the other. One of the most important safety features of this reactor type is the self-moderating property of the core because of the Zr-H combination. This moderator has a so-called negative temperature coefficient in regard to absorbing neutrons. This means when the reactor is over-critical (more fission reactions than needed to keep the chain reaction constant take place, the number of fissions increases exponentially) the fuel elements and the moderator heats up as a result. This temperature increase however results in a less efficient moderation of neutrons by the Zr-H causing a decrease in available neutrons that can take part in the reaction consequently stabilising the reactor. [25]

A white neutron beam is a beam that has the form of a Maxwell-Boltzmann distribution. It consists of neutrons directly from the core of the reactor after moderation. At the ATI the thermal spectrum has a temperature of 303 K which is equal to speeds of $2737\,\mathrm{m\,s^{-1}}$ or a mean kinetic energy of 26.1 meV [12, p.23]. The 'Thermal White Neutron Beam Facility' (TWB) at the Atominstitut providing such a spectrum is located at the beamline 'B' of the TRIGA reactor. The initial white spectrum from the reactor is modified somewhat due to the presence of a sapphire and a Bi-crystal filter for fast neutrons, as well as a gamma ray filter aimed to minimise distorting effects in the measurements. For more detailed information concerning the neutron flux spectrum and the protective measures taken at the beamline refer to the work of W. Mach [12].

Currently, the most powerful source of neutrons is the high-flux reactor at the Institute Laue-Langevin (ILL) in Grenoble, France [26].

2.2.3 Spallation

Another way to obtain free neutrons is a process called spallation. When highly energetic particles with about 1 GeV hit a nucleus they can deposit a lot of their energy and induce the nucleus' disintegration into many smaller particles such as neutrons, protons and light elements. When heavier elements are targeted and form lighter ones, more free neutrons are produced as explained in *Section* 2.2.2. Elements like tungsten can set free more than 20 neutrons per reaction. The incident particles, usually protons, are produced in particle accelerators. Since these particles are only produced in bunches, the neutron source can usually only operate in a pulsed mode. However, it is possible to create a continuous source through spallation by pulsing neutrons at very high frequencies and increasing the mean residence time in the moderator causing different neutron generations to mingle (e.g. *SINQ* in Villigen, Switzerland).

Some of the world's most important spallation sources are *nTOF* at *Cern* in Geneva, Switzerland, *ISIS* at *Rutherford Appleton Laboratory* in Harwell, Great Britain or *SNS* at *Oak Ridge National Laboratory* in Oak Ridge, United States of America. In addition, the *European Spallation Source (ESS)* is currently under construction in Lund, Sweden and is to be the world's most powerful spallation source. First experiments are scheduled to commence in 2023 [27].

2.3 Polarisation of neutrons

Neutrons can be polarised because of their interaction with the magnetic force and the strong nuclear force. When scattering, it is one of these two mechanisms that play the most important role. This fact can be put to use when considering that the two effects can superimpose to augment or reduce scattering, sometimes to the point where the two effects act equally to annihilate it altogether. Some materials show these properties where the two forces have nearly the same strength permitting to polarise a neutron beam [28], [29].

An important parameter when assessing the effectiveness of a polariser is the polarising efficiency P. It may be written as

$$P = \frac{N_\uparrow - N_\downarrow}{N_\uparrow + N_\downarrow} \ , \tag{2.5}$$

with $N_\uparrow$ and $N_\downarrow$ being the numbers of spin neutrons in the respective ($\uparrow$) or ($\downarrow$) state of the transmitted beam. The aim is to maximise the number of neutrons polarised parallel to the polarising material and minimising neutrons with an antiparallel magnetic momentum.

In addition, the loss of intensity must be considered. This depends on the angular acceptance of the polariser and the reflectivity of the crystal or mirror, or in the case of polarising filters, the transmittance [17, p.98].

2.3.1 Polarising crystals

Monochromator crystals work using the Bragg diffraction on the (hkl) planes at a mean reflection angle $\bar{\theta}_b$. The condition for constructive interference of an incident beam is given as

$$n\,\bar{\lambda} = 2\,d_{hkl}\,\sin\bar{\theta}_b \ , \tag{2.6}$$

with $\bar{\lambda}$ being the mean wavelength, d_{hkl} the interplanar distance of the crystal and n the order of reflection. This can be used to monochromatise a white beam. It is desired that higher-order reflections are absent or adequately negligible.

To take this one step further and polarise the reflected, monochromatic neutrons, a vertical magnetic field needs to be applied to the ferromagnetic single crystal. When the incoming neutrons are reflected on the magnetised (hkl) plane and the nuclear and magnetic forces acting on them are equal, the resulting beam will be monochromatic and polarised [17, pp.8, 98–100].

However, in order to have equal nuclear and magnetic forces act on the neutrons, only a few materials are known to satisfy the necessary condition almost exactly [30]. The most used material by far is the so-called 'Heusler alloy' (Cu_2MnAl) reflecting on the (111)-plane with an interplanar spacing of $d_{111} = 3.453\,\text{Å}$ [17, p.99-102].

2.3.2 Polarising filters

Polarising filters selectively remove one of the spin states of an unpolarised incident beam through either scattering or absorption, and permit the other state to be transmitted unobstructedly.

One way to accomplish this is by using a magnetised iron filter. This method depends on the interference between the magnetic and the nuclear scattering when the neutrons travel through the polariser, a magnetised polycrystalline block [17, pp.104].

Another method would be to exploit spin-dependent absorption effects of polarised nuclei as filters. Here, the absorption cross-section of the polarised nuclei and the nuclear resonance energies are key to separating the two different spin states [17, pp.106].

The last method is the polarised-proton filter which is effective for energies around 1 keV and relies on the spin dependence of nuclear scattering [17, p.111].

For more details on polarising filters refer to W. G. Williams [17].

2.3.3 Polarising mirrors

The method of polarising neutron beams by using mirror reflection became prominent after D. J. Hughes and M. T. Burgy [32] successfully produced a completely polarised beam using cobalt mirrors in 1951.

Polarising mirrors take advantage of the reflection of all neutrons with an incident angle smaller than a critical angle θ_c. The effectiveness of these mirrors strongly depends on the critical ratio θ_c/λ_c, with λ_c being the critical wavelength. For ($\uparrow$) spin neutrons this ratio is very small and usually only reaches $\sim 1.8\,\text{mrad}\,\text{Å}^{-1}$ [17, pp.115-125].

An external magnetic field aligns the magnetic momenta of the reflective material

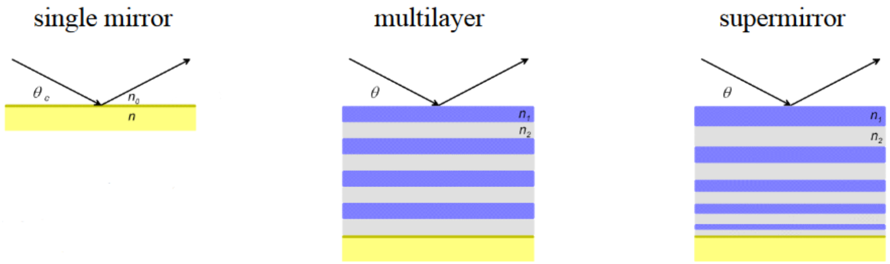

FIG. 2.1 – Working principle of different neutron mirror types [31].

to the point of magnetic saturation making the reflections spin dependent. This is usually achieved by a set of permanent magnets. As discussed earlier, the nuclear and magnetic scattering have to be of similar magnitude in order to be able to polarise.

Multilayer mirrors are mirrors consisting of one magnetic and one non-magnetic material responsible for reflecting neutrons. These materials are applied onto a glass or silicon substrate pairwise resulting in an alternating structure. To avoid direct transmission of neutrons without a mirror reflection, the carrier material is slightly bent. At the bottom of these multiple layers a neutron absorber such as cadmium or boron is administered to prevent transmitted (↓) spin neutrons from scattering further, possibly finding a way to the detector and deteriorating the results of the measurement. Usually, one polarising mirror is made up of numerous, parallel multilayer sheets. The multi-bilayer system produces another Bragg-reflection for the glancing angle fulfilling the condition $\frac{\lambda}{2\,d_{hkl}}$ [33].

Supermirrors use this technology and improve the reflective efficiency by decreasing the thickness of the layers as the penetration depth increases creating a quasi-continuum of 'pseudo-Bragg' reflections.

The concept of polarising supermirrors was first introduced by F. Mezei [34] in 1976. This allows for a much higher critical angle θ_c (larger by a factor 4–6 [34]) compared to normal multilayer mirrors meaning that higher efficiency rates can be achieved. Common materials can be alternating layers of the pure isotopes ^{58}Ni and ^{62}Ni, a combination of Fe and SiGe [35] or, in the case of the mirrors used during this work, Co and Ti.

For a wide range of thermal wavelengths, the reflectivity below the critical angle θ_c is not perfect but can reach more than 90 %. Often, the 'm-value' is introduced for supermirrors, defined as

$$\theta_c = m\,\theta_{c(\mathrm{Ni_{nat}})} \quad , \tag{2.7}$$

with $\theta_{c(\mathrm{Ni_{nat}})} = 1.73\,\mathrm{mrad}\,\mathrm{\mathring{A}}^{-1}$ being the critical angle of reflection of a flat surface coated with natural nickel [12, p.88]. In FIG. 2.2 one can see the m-value of a supermirror plotted over the reflectivity. According to EQ. (2.7) a value of $m = 1$ would mean the reflectivity of the supermirror is equal to that of a flat surface of nickel, a value of $m = 2$ a critical angle θ_c of twice the angle of natural nickel and so forth.

The red line shows the reflectivity for one reflection on a single mirror of nickel. The efficiency strongly decreases at $m = 1$. For a supermirror the different thicknesses of the reflective pairs mentioned earlier would reflect neutrons for one special angle in shades of blue, in combination creating a region after the regime of total reflection where the reflectivity stays almost constant and only sharply decreases at a far steeper angle.

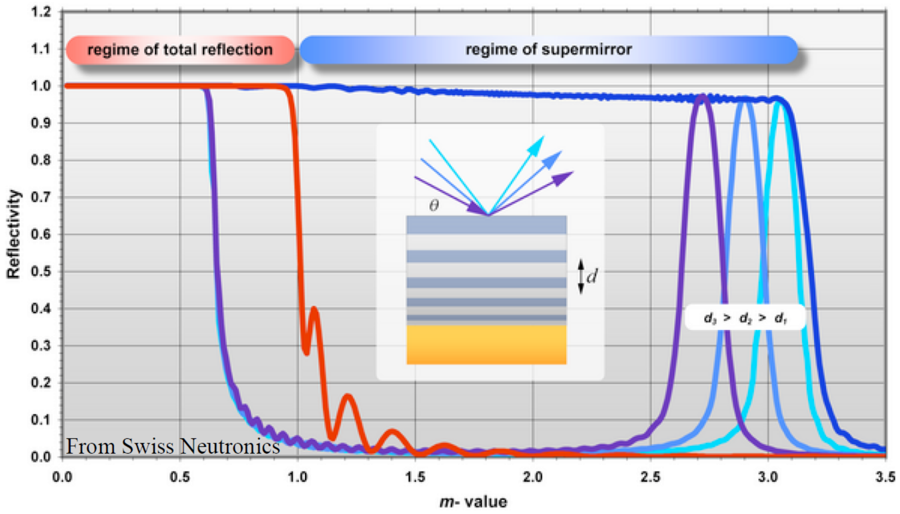

FIG. 2.2 – A single mirror reflection (red) compared with a supermirror reflection (shades of blue) [31].

2.4 Spin flippers

A spin flipper is a device used to invert the polarisation of an ensemble of neutrons. The (↑) and (↓) states can be flipped to the respective other state. Sending a polarised beam through a spin flipper can cause the polarisation vector of that beam to be inverted and this plays an important role when trying to analyse polarised neutron beams. The beam that is to be inverted has to fulfil a resonance condition or a spin flip condition to assure the success of the process. Typically, magnetic fields are used to achieve this.

In a magnetic field B (in this context the guiding field strength will be labelled as B_0), the spin with a magnetic momentum μ rotates around the direction of said magnetic field with the Larmor frequency ω_L. This precession frequency depends on the gyromagnetic ratio γ:

$$\omega_L = |\gamma| \, B_0 \tag{2.8}$$

with

$$\gamma = g\frac{\mu}{\hbar} \tag{2.9}$$

where g is the neutron g-factor.

The guiding field is needed to prevent a depolarisation of the beam. In addition, an alternating magnetic field B_1 performs the actual spin flip through an adiabatic or non-adiabatic process. Only when complying with the resonance condition the spin of the neutron beam can be inverted.

It is essential that all magnetic stray fields in the region of the spin flip are minim-

ised since this reduces the transition probability of the neutrons due to the increase in their Larmor precession frequency.[17, p.130].
It is possible to calculate the spin flip efficiencies of the spin flippers when using an experimental setup where two different spin flippers are installed in a polarised neutron beam. Through the performance of four separate time-of-flight measurements the efficiencies e_1 and e_2 of each device as well as the overall degree of polarisation $P = P_P P_A$ through the solving of equations Eq. (2.10) – Eq. (2.12) (see J. Bosina [11, p.13]) is possible.

$$\frac{N_{10}}{N_{00}} = \frac{1 - e_1 P_P P_A}{1 + P_P P_A} \Rightarrow e_1 = \frac{N_{01} - N_{11}}{N_{10} - N_{00}} \tag{2.10}$$

$$\frac{N_{01}}{N_{00}} = \frac{1 - e_2 P_P P_A}{1 + P_P P_A} \Rightarrow e_2 = \frac{N_{10} - N_{11}}{N_{01} - N_{00}} \tag{2.11}$$

$$\frac{N_{11}}{N_{00}} = \frac{1 + e_1 e_2 P_P P_A}{1 + P_P P_A} \Rightarrow P_P P_A = \frac{(N_{01} - N_{00})(N_{00} - N_{10})}{N_{10} N_{01} - N_{00} N_{11}} \tag{2.12}$$

N_{00}, N_{10}, N_{01}, N_{11} represent the number of transmitted neutron if both spin flippers are turned off (00), one is turned on (10 or 01), or both turned on (11).

In general, two different types of spin flippers can be identified: broad-band and narrow-band spin flippers.

2.4.1 Broad-band spin flippers

Broad-band flippers are able to change the spin state of incident neutrons over a wide range of wavelengths. Through an extremely fast, non-adiabatic change of the direction of the magnetic field in a short distance compared to the distance a neutrons covers during a complete Larmor rotation a spin flipper can be created. This behaviour is taken advantage of when using broad-band flippers such as the non-adiabatic coil flipper and current-sheets. In this section only the current-sheet will be discussed. For information on the non-adiabatic coil flipper refer to D. J. Hughes and M. T. Burgy [32], or for a more general overview, W. G. Williams [17, pp.129].

Current-sheets

Current-sheets usually consist of a guiding field, a compensation field and the current-sheet itself. The spin flip efficiency is nearly independent of the neutrons' wavelengths. In the simplest setup the current-sheet is represented by a thin sheet with densely arranged current-carrying wires parallel to the direction of the

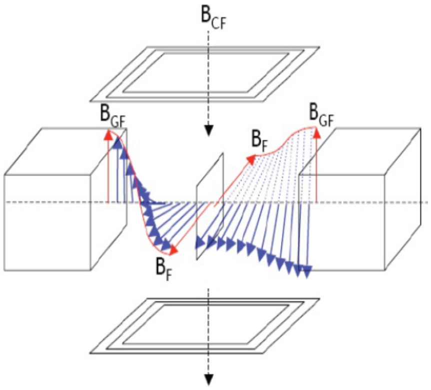

FIG. 2.3 – Schematic evolution of the neutron spin (blue) as it passes the current-sheet from left to right influenced by its magnetic field (red). B_{GF} represents the guide field, B_F the flipper field, and B_{CF} the compensation field when the flipper is turned off [30].

guiding field (see FIG. 2.3). When a neutron approaches the spin flipper its spin is stabilised by the guiding field. The closer it gets to the flipper the more that field cancels out with the compensation field designed to oppose the guiding field. With the additional magnetic field created by the current flowing through the metal sheet perpendicular to the outer fields the spin keeps aligning with the magnetic field adiabatically. When it reaches the current-sheet it is completely parallel to the magnetic field. As soon as it passes through the thin sheet however, the magnetic field it suddenly experiences lies anti-parallel to its spin because the change happens too fast for the neutron to permit an alignment to the field. Subsequently, the magnetic field of the spin flipper and the compensation field lose their influence as the neutron continues to move forward and aligns anti-parallelly to the outer magnetic field having now completed a π-flip.

2.4.2 Narrow-band spin flippers

These spin flippers are used to select specific wavelengths from the incident neutron spectrum. Ideally, all other wavelengths should be suppressed and filtered. Representatives of such narrow-band flippers are adiabatic coil flippers and radiofrequency spin flippers.

Radiofrequency (RF) spin flipper

The concept of the RF spin flipper was first introduced by L. W. Alvarez and F. Bloch [36]. It stands out due to the fact that its explicit time-dependant inter-

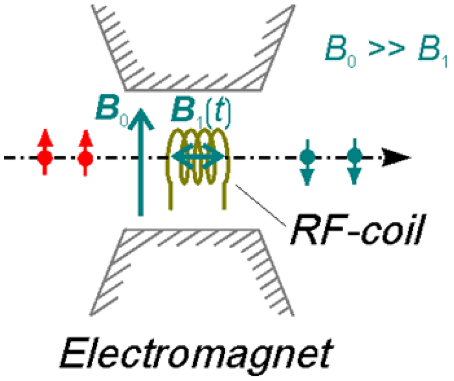

FIG. 2.4 – Schematic evolution of the neutron spin in an RF coil flipper [30].

action changes the energy but not the state of movement of the neutron. When entering a stationary guide field B_0, not only the expected value of the kinetic energy of the neutron is changed (resulting in acceleration or deceleration of the particle), but also its potential energy which causes a Zeemann splitting.

If an interaction with a time-dependant potential takes place – in the case of an RF spin flip by changing the Zeemann level – the distribution of the momenta remains constant. However, this is not the case for the potential energy. The total energy is conserved and because the potential energy returns to its original value, a change in the kinetic energy must have taken place. The amplitude B_1 has to be matched with the incident velocity of the neutron to achieve a spin flip.

The length of the RF spin flipper is dependent on the adiabatic resonance condition, that has to be fulfilled for a spin flip. This resonance condition makes the device highly sensitive to changes of the guide field B_0 [30], [9, p.14].

Direct-current (DC) coil flippers

The concept of the DC-coil flipper was first introduced by F. Mezei in 1972 [37]. Using thin, rectangular coils a rotation of the neutron's spin respective to the guiding field B_0 could be performed. Such devices performing a π-flip of the neutron spins are commonly known as Mezei spin flippers.

Suppose one knows the magnitude of the guiding field B_0 and can compensate it with a compensation coil around the DC-coil flipper. If a magnetic field inside the flipper with a strength B_F is set, the internal field will be pointing exactly into the y-direction. When a z-polarised neutron beam travelling along the x-axis penetrates the side of the flipper coil it experiences a sudden, non-adiabatic transition before the polarisation vectors of the individual neutrons begin to rotate around the internal magnetic field in the y-direction. If a neutron fulfils exactly half a Larmor precession its spin will be pointing precisely into the -z-direction when exiting the DC-coil flipper now having performed a π-rotation.

It is also possible to perform such a spin flip when using two separate DC flippers, the first one creating an internal magnetic field inclined at a 45° angle from the y-direction, the second one a field with an angle of $-45°$. For such a configuration each coil causes a $\frac{\pi}{2}$-flip.

The resulting magnetic field strength $\vec{B}_{\mathrm{R}}$ at any position can be calculated if the individual components (guide field $\vec{B}_{\mathrm{G}}$, flip-coil field $\vec{B}_{\mathrm{F}}$ and compensation field strength $\vec{B}_{\mathrm{C}}$) are known, as shown in Eq. (2.13).

$$\vec{B}_{\mathrm{R}} = \vec{B}_{\mathrm{G}} + \vec{B}_{\mathrm{F}} + \vec{B}_{\mathrm{C}} \tag{2.13}$$

This means that under the resonance condition

$$d = \frac{\pi v}{\omega_L} = \frac{\pi v}{|\gamma \vec{B}_{\mathrm{R}}|} \quad , \tag{2.14}$$

with d being the width of the coil, the spin of the neutrons in inverted and subsequently points into the negative z-direction after having traversed the DC flipper. A visualisation can be found in Fig. 2.5.

Using this kind of spin flipper has some important advantages, as they are simple to construct, easy to control electronically and the position of the spin flip can be located without great difficulty [30], [9, pp.14].

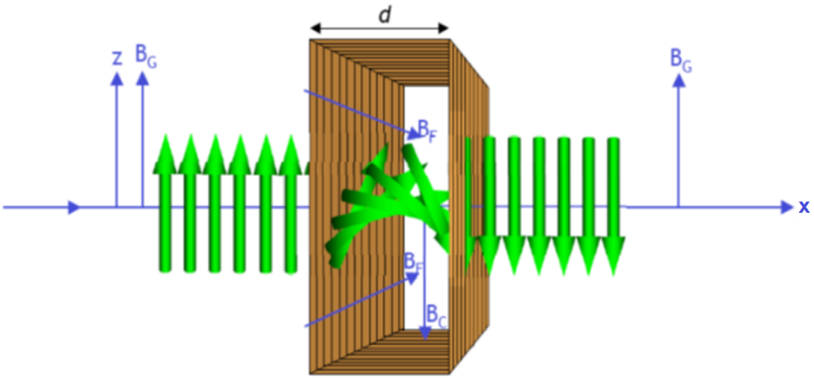

Fig. 2.5 – Schematic evolution of the neutron spin in a DC-coil flipper [30].

2.5 Choppers

Choppers can fulfil two different functions, firstly pulsing steady neutron beams, and secondly, selecting specific wavelengths. For a pulsed source usually only wavelength selection is needed as the neutrons are already produced in pulses. As previously discussed, neutron sources like nuclear research reactors produce a

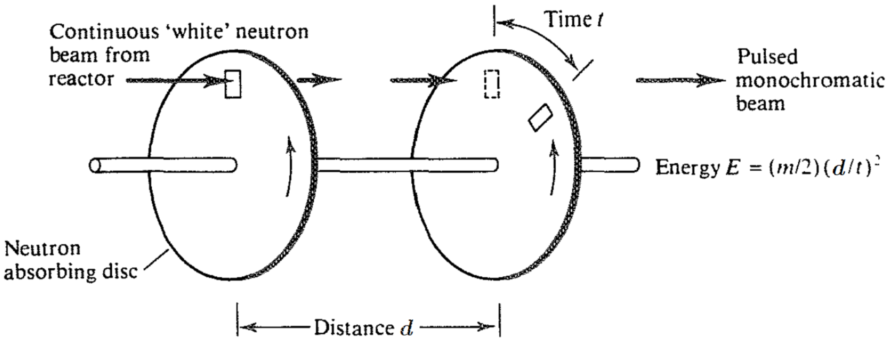

FIG. 2.6 – Principle of neutron wavelength selection on a continuous neutron source using a mechanical disc chopper and the neutron time of flight [17, p.7].

continuous flux of particles with different wavelengths. To be able to distinguish between such neutrons and their respective wavelengths the beam can be chopped up into short pulses. The simplest way to subsequently determine the velocity of a neutron is to measure their flight time as they traverse a known distance, the time-of-flight (TOF) method.

Commonly, fast-spinning, magnetically pivotable cylinders made of neutron absorbing material with recesses for the wavelength selection are used as choppers.

2.5.1 Disc choppers

In FIG. 2.6 a type of disc chopper can be seen. A continuous white beam from a nuclear reactor hits the first chopper disc and is parsed into pulses allowing for the transmission of neutrons for a limited period of time depending on the angular velocity of the disc. The opening of the second disc only transmits neutrons, if these neutrons pass the distance d in the time t since only then they are permitted to pass the second disc. This leads to a selection of neutrons with an energy of

$$E = \frac{m}{2}\left(\frac{d}{t}\right)^2 \quad , \tag{2.15}$$

or with a wavelength of

$$\lambda = \frac{2\,\hbar c}{m}\left(\frac{t}{d}\right)^2 \quad . \tag{2.16}$$

The smallest difference in wavelengths $\Delta\lambda$ that can be distinguished at a wavelength λ mainly depends on the size of the chopper window, the rotational speed of the discs and its constancy. Decreasing the window size can lead to a sharper line but will affect the count rate negatively. Usually such systems can select wavelength ranges of $\Delta\lambda/\lambda \sim 1 - 10\,\%$ [9, pp.9].

2.5.2 Fermi-choppers

Fermi-choppers were first built by Fermi *et al.* [38] in 1947 and have since then improved. Their basic concept involves a stack of vertically arranged, alternating aluminium and cadmium layers in a rotating cylindrical shape. When turning at a pre-defined frequency, this cylinder would permit neutrons to pass the chopper when the stack was aligned parallel to the neutron beam. Otherwise, it would absorb any neutrons from the source due to the absorptive characteristics of cadmium [12].

2.6 Neutron detection

Neutrons can generally be detected by taking advantage of nuclear reaction that cause prompt charged particles such as protons, α-particles and others. This method can be used especially effectively when dealing with neutron energies below 0.5 eV, the so-called 'cadmium cutoff'. In such cases the wavelengths, or energies, of the neutrons are usually determined by crystal spectrometers or by time-of-flight measurements [39, p.505].

For information on neutron detectors for energies above 0.5 eV refer to G. F. Knoll [39] as a discussion would exceed the scope of this work.

When designing a detector and choosing the active detector material, several factors have to be taken into account. The cross section for the target nuclide has to be as large as possible to be able to build small and efficient detectors. The material targeted should also be easily available either through high abundance, or through economically reasonable enrichment of said isotope. Another important aspect is the fact that intense gamma fields commonly surround areas where neutron detections take place. However, these high-intensity electromagnetic radiation should be discriminated and neutron events filtered. Here, the Q-value of the reaction is important since it determines the energies that are given to the products of the induced reaction. The higher the Q-value, the higher the energies of the reaction products through the interaction, subsequently greatly assisting in the distinction between neutron and non-neutron events. [39, pp.505]

Common reactions for the detection of slower neutrons all result in the measurement of heavy charged particles, such as recoil nuclei, protons, alpha particles and fission fragments. The kinetic energy of these exothermic reactions are determined solely by their Q-value since the incoming kinetic energies of the neutrons are negligible [39, pp.505].

Due to losses based on the geometry and materials of the detector the full energy of the reaction products can not always be deposited in the active area of the detector and lower energies for these products will also be measured, despite having been

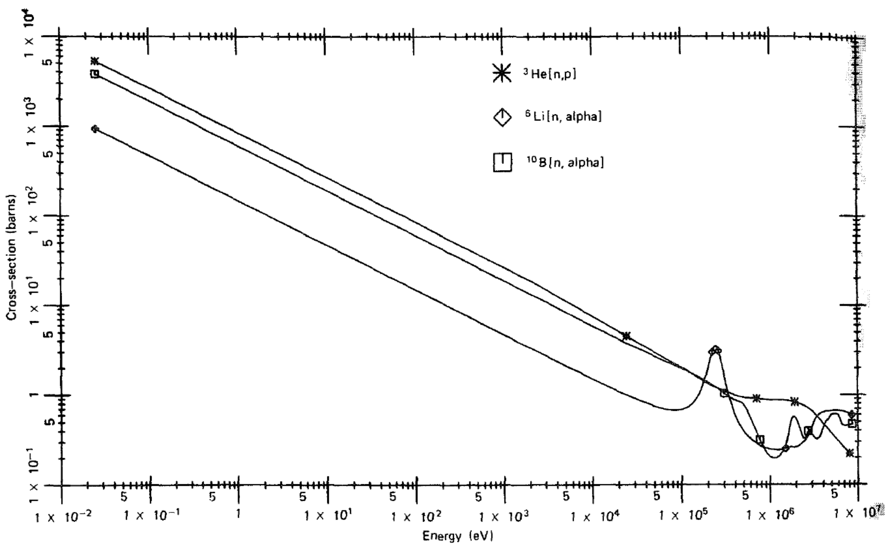

Fig. 2.7 – Cross section versus the neutron energy for some reactions of interest in neutron detection [39, p.508].

caused by a neutron event [39, p.506].
Such neutron detectors can be realised as proportional tubes. The tubes are gas-filled detectors first developed in the late 1940s. They are based on the principle of ion multiplication to enhance the charge of originally formed ion pairs. The achieved pulse heights are significantly larger than for ionisation chambers under the same conditions. They are commonly used in scientific areas where the number of incident radiation causing the formation of ion pairs would otherwise be too small and as such are often used as neutron detectors. When proportional tubes are sufficiently large, all resulting reaction products can deposit their full energy in the active area of the detector. When the geometry of the detector is chosen to be smaller for practical or economical reasons, this can produce the so-called 'wall effect'. If for example one of the produced particles from the reaction hits the detector wall before being able to deposit its entire energy, this leads to a decrease in the deposited energy for said particle altering the pulse height spectrum towards lower energies [39, p.511].

2.6.1 BF_3 detector

The BF_3 proportional tube is widely used for the detection of slower neutrons. Boron trifluoride constitutes the target gas for the conversion of slow neutrons through the $^{10}B(n,\alpha)$ reaction

$$ {}^{10}_{5}B + {}^{1}_{0}n \Rightarrow {}^{7}_{3}Li + {}^{4}_{2}\alpha \qquad (2.17) $$

with Q-values of 2.792 MeV and 2.310 MeV for the respective ground and excited state of ${}^{7}_{3}\mathrm{Li}$. In addition, it is also the responsible component for the ion multiplication as a proportional gas. For thermal neutrons, the cross section of the ${}^{10}\mathrm{B}(\mathrm{n},\alpha)$ reaction amounts to 3837(9) b [40]. As can be seen in FIG. 2.7, the cross section falls fast with increasing neutron energies proportionally to $1/v$. The released energies from the mentioned reaction in the range of a few MeV makes it rather impossible to determine the original neutron energy ($\sim 25\,\mathrm{meV}$ for thermal neutrons) [39, p.507–509].

BF_3 proportional tubes are usually constructed using cylindrical cathodes on the outside and thin wire anodes inside with an aluminium casing. Typical operational voltages can be around 2 – 3 kV for anode diameters of 0.1 mm [39, p.513].

2.6.2 ^{6}Li detector

The ${}^{6}\mathrm{Li}(\mathrm{n},\alpha)$ reaction is another process that can be used for neutron detection. The nuclear reaction

$$ {}^{6}_{3}\mathrm{Li} + {}^{1}_{0}\mathrm{n} \Rightarrow {}^{3}_{1}\mathrm{H} + {}^{4}_{2}\alpha \tag{2.18}$$

has a Q-value of 4.78 MeV, with 2.73 MeV of the total energy deposited on the triton and 2.05 MeV on the α-particle. The cross section for this reaction is 940(4) b [39, pp.507].

The higher Q-value of the lithium reaction compared to that of boron shows important advantages when it comes to discriminating gamma pile-up and other low energy events. In addition, the fact that the lithium reaction always produces the same amount of energy unlike the boron reaction with a ground and an excited state results in a single peak for each event. Commonly, scintillators containing lithium are used and sometimes these devices can be enhanced by adding small amounts of europium to increase the scintillation output. A commercially available detection device uses lithium iodine crystals which are typically found hermetically sealed due to their hygroscopic properties. The high density of these crystals, especially compared to neutron detectors using gas, allows for compact but still highly efficient detector geometries [39, pp.517].

2.6.3 ^{3}He detector

^{3}He, a gas, is also commonly used to detect slow neutrons through the following reaction

$$ {}^{3}_{2}\mathrm{He} + {}^{1}_{0}\mathrm{n} \Rightarrow {}^{3}_{1}\mathrm{H} + {}^{1}_{1}\mathrm{p} \tag{2.19}$$

with a Q-value of 0.764 MeV. The cross section of 5333 b for thermal neutrons is significantly higher than that of ^{10}B or ^{6}Li and it also shows a $1/v$ energy depend-

ence like the previously discussed reactions. However, the high cost and reduced availability of commercially obtainable ^{3}He poses a problem for its usage in some applications [39, pp.508].
The ^{3}He proportional tube is an appealing alternative to the previously mentioned solutions of detecting neutron events due to its high cross section. The fact that it can only be used in gaseous form poses some disadvantages since larger active detector areas are needed. This also means that the range of the reaction products increases and, as mentioned before in *Section* 2.6.1, the wall effect can play an important role in the neutron detection and can cause plateau shapes in the pulse height spectra essentially impeding the discrimination of low-level gamma and real neutron events. Additionally, this effect is far more prominent for ^{3}He than BF_3 tubes at equal size and gas pressure considering its comparably low atomic mass. To counteract these unwanted effects a few steps can be taken. Firstly, maximising in the tube diameter would evidently improve the measurement. Secondly, increasing the pressure in the tube as well as adding small amounts of heavier gases to the ^{3}He to impede the range of the reaction products can significantly improve results. The helium tubes can operate with much higher pressures than BF_3 counters and are preferred for uses in which a maximum efficiency of the detector is needed or desired [39, pp.518].

2.7 Drabkin resonator

The concept of a new type of neutron resonator was first introduced by G. M. Drabkin in 1963 [2]. The idea was to be able to monochromatise a polarised neutron beam by using an accordion-pleated aluminium foil with the length L and a spatial period of $2a$ [3]. When running a current through the resonator foil this produces a spatially alternating, transversal, static magnetic field B_1 – also called resonator field – perpendicular to the incident neutron beam. However, observed from the neutron's rest frame as it passes through the aluminium meander it will perceive the magnetic field as alternating and time-dependent. The device has similarities with the radio-frequency flipper discussed in *Section* 2.4.2, with the distinction that for a Drabkin resonator every neutron has its own resonance frequency depending on its wavelength λ [3], [41].
In addition to the B_1 field, a guide field B_0 – in this context also called selector field due to its function of selecting specific wavelengths – is applied across the entire setup causing the neutrons to rotate around the direction of the external magnetic field with the Larmor frequency (see Eq. (2.8)).
When passing through the resonator every single neutron experiences the rotation

frequency

$$\omega(\lambda) = \frac{h\,\pi}{m} \cdot \frac{1}{a\,\lambda} \tag{2.20}$$

dependent on the wavelength of the neutron, with a representing half a resonator period (see FIG. 2.8).
In a resonator of a length L with an alternating field B_1 and a selector field B_0 a complete π spin flip takes place at a resonance frequency

$$\lambda_0 = \frac{h\,\pi}{m|\gamma|} \cdot \frac{1}{a\,B_0} \tag{2.21}$$

if the amplitude condition

$$\frac{B_1}{B_0} \cdot \frac{L}{a} = (2\,k+1)\,\frac{\pi}{2} \qquad (k = 0, 1, 2, \dots) \tag{2.22}$$

is met. The parameter k indicates the order of the resonance. For $k = 0$ one single spin flip is obtained – for example a transition from spin up to spin down (↑↓). Multiple spin flips are possible, so for a value of $k = 1$ three spin flips (↑↓↑↓) would occur and so forth.
Presuming that the incoming neutron beam has been fully polarised in the (↑) state, this leads to a neutron beam with different spin states that are then inverted for all wavelengths using a broad-band spin flipper such as a current-sheet. Thereupon, the neutrons reach the second polariser that only permits neutrons having previously performed a spin flip in the resonator to pass. As a result, one receives a polarised neutron beam of a selected wavelength (see FIG. 2.8) [10, pp.9], [11, pp.16].
In case $B_0 \gg B_1$ one can calculate the spin flip probability for a neutron passing through the Drabkin resonator analytically by solving the Pauli equation for the magnetic moment in a spatially time-dependant magnetic field resulting in

$$W(\lambda) = \frac{\beta^2}{(\Delta\lambda/\lambda)^2 + \beta^2} \cdot \sin^2\left(\frac{\pi}{2}\,\frac{\lambda\,L}{a\,\lambda_0}\,\sqrt{(\Delta\lambda/\lambda)^2 + \beta^2}\right) \tag{2.23}$$

with

$$\Delta\lambda = \lambda - \lambda_0 \tag{2.24}$$

and

$$\beta = \frac{2}{\pi} \cdot \frac{B_1}{B_0} \ . \ [5] \tag{2.25}$$

A complete spin flip for the neutrons takes place if the resonance condition

$$\Delta\lambda = 0 \tag{2.26}$$

and the amplitude condition (EQ. (2.22)) are fulfilled. For $k = 0$, the wavelength resolution in regard to the half width at half maximum (HWHM) becomes

$$\frac{\Delta\lambda_{1/2}}{\lambda} \cong 1.6\frac{a}{L} = 0.8\frac{1}{N} \tag{2.27}$$

with

$$N = \frac{L}{2\,a} \tag{2.28}$$

representing the number of spatial magnetic field periods [5].

From EQ. (2.27) it is easily deductible that by decreasing the resonator period a and/or increasing the resonator length L higher resolutions can be achieved by the Drabkin resonator.

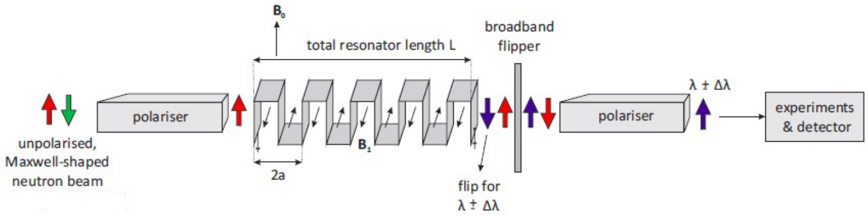

FIG. 2.8 – Arrangement of a Drabkin neutron resonator [10].

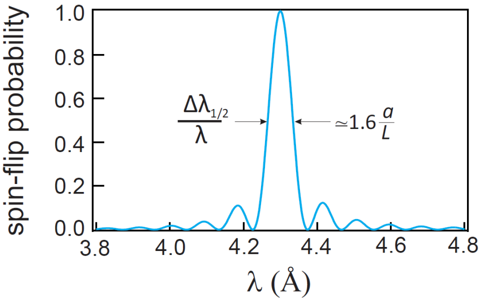

FIG. 2.9 – Spin flip probability dependent on the neutron wavelength λ. A full spin flip is performed by neutrons with the resonance wavelength λ_0 [6].

As can be seen in FIG. 2.9, the spinflip probability shows a distribution with side maxima that are generally unwanted. These can be eliminated using one of the following approaches:

Firstly, one could use two different resonators adjusted so that the side maxima of the initial distribution is superimposed with the minima of the second resonator [42]. Secondly, an approach taking advantage of the fact that the Fourier transformation of the spin flip probability corresponds to the spatial magnetic field distribution of the resonator can be exploited. The accordion-pleated aluminium foil, essentially a rectangular function, produces a Fourier transformation proportional to $\sin^2(x)/x^2$.

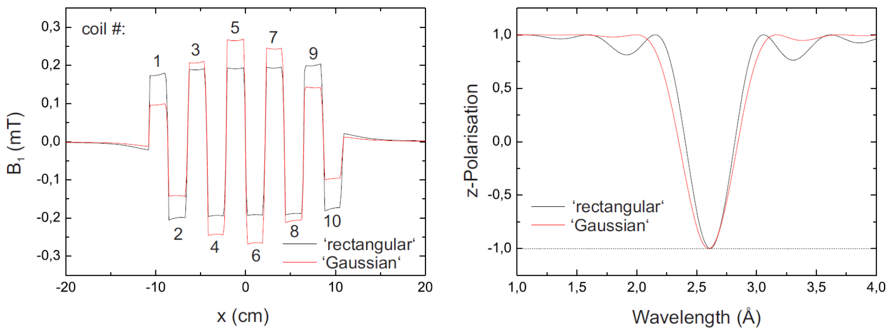

FIG. 2.10 – A simulation of different shaping for the alternating field B_1 for $N = 10$ individual coils performed by C. Gösselsberger [6, p.71].

If now the rectangular foil shape is replaced by a Gaussian-shaped foil and hence produces a Gaussian magnetic field distribution, the Fourier transformed function will again be a Gaussian shape [43] consequently eradicating the problem of the side maxima (see FIG. 2.10) [6].

It is also possible to switch the entire resonator on and off at some pre-defined frequency allowing for a pulsed mode essentially replacing the function of a chopper, since the broad-band spin flipper would hinder any unflipped neutrons from passing through the second polariser.

2.7.1 The 'Badurek-type' resonator

In 1991, G. Badurek *et al.* [4] published the idea of an advanced Drabkin resonator, which later became known as a 'Badurek-type' resonator. The fundamental idea was to replace the accordion-pleated single foil by an arrangement of individual coils that can be controlled separately. Each coil has its own power supply controlling its magnetic field and has the capability to be switched on and off individually with a metal-oxide-semiconductor field-effect transistor (MOSFET).

Advantages of such a resonator type include the flexible shaping of the alternating magnetic field B_1 and shorter pulse lengths. Since the variation of the field strengths for each coil is possible, no special geometry is needed since the electrical currents can easily be set by power supplies adjusted by a program or the experimenter.

As mentioned in the previous section, a pulsed mode replacing a chopper is possible. This function can now be improved by reducing the number of coils that are switched on at a time. Very short pulses can be achieved by implementing the so-called 'travelling wave mode' (TWM) [5]. Since individual coils can be operated separately, a higher resolution can be achieved by following a well-defined group of neutrons through the resonator. For example, it is possible to switch on only

one coil in the exact moment the neutron pulse passes through it and turn it off as soon as the ensemble of neutrons has advanced to the next coil which is now being switched on. Thereafter, the next coil is switched on and the previous one off essentially following the neutron pulse through the length of the resonator. This will result in a high resolution of the pulse, now depending on the number of magnetic field periods, in this case represented by the single coils (see Eq. (2.27)).
The scheme of the 'Badurek-type' resonator can be seen in Fig. 2.11 [5].
Limitations of the concept are henceforth not the geometry but switching times of the MOSFETs as well as the electrical currents that can be supplied and problems resulting from these issues such as heat dissipation and exact timing.

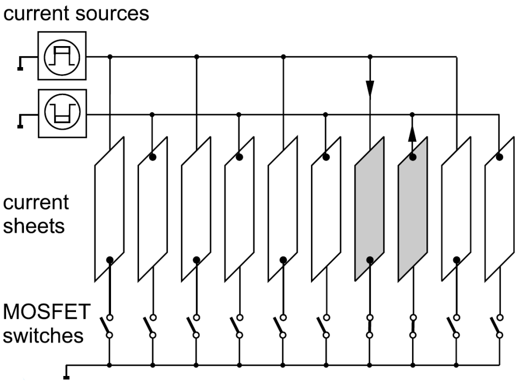

Fig. 2.11 – The working principle of a 'Badurek-type' resonator [5].

The Monopol project

The Monopol project was initiated at the Atominstitut of TU Wien around G. Badurek and E. Jericha together with C. Gösselsberger with the goal to build a prototype of such an advanced Drabkin resonator [6].
Since then, prototype 1.0 as well as the next generation prototypes 2.0 and 3.0/3.1 have been developed with the aid of many students. While prototypes 1.0 and 2.0 were tested on the dichromatic beamlines of the Atominstitut, Monopol 3.1 was developed to tailor a white VCN beam at the ILL in Grenoble. The experiments in France were performed by E. Jericha, S. Baumgartner, B. Berger, G. Badurek and R. Raab in summer 2013, and by E. Jericha, J. Bosina and W. Mach in September 2014. For detailed information on the history and development of the Monopol project up to 2005 refer to J. Bosina [11, p.21-25].
During his PhD thesis, W. Mach *et al.* established a new thermal white beam site at the TRIGA reactor of the ATI [12], [44].
Experiments at the 'Thermal White Neutron Beam Facility' (TWB) are among the

first scheduled experiments for the next-generation resonator Monopol 4.0 currently under construction.

This thesis should path the way for the Monopol experiment in demonstrating that polarising the beam, flipping certain wavelengths with the help of DC-coil flippers imitating the resonator, inverting the polarisation of the complete thermal neutron spectrum by the use of a current-sheet and monochromatising the beam is possible.

3 Experimental Setup

In the first part of this chapter, the individual components and their impacts on the main polarisation experiments at the white neutron beam of the TRIGA reactor at the Atominstitut will be described.
In the second part, the different experimental configurations of these components will be explored and their expected effects on the spectrum outlined.

3.1 Experimental components

3.1.1 Supermirrors

The neutron research group at the Atominstitut is currently in possession of four grey polarisers purchased from the Institute of Nuclear Physics, Gatchina/Russian Federation about 20 years ago. They are labelled 'P' as well as 'I' – 'III'. Two of these identically constructed supermirror polarisers were used for the experiments, one of them can be seen in Fig. 3.1.
The first polariser used in the experiments described in the following chapters was polariser 'II', from now on referred to simply as 'polariser' or 'POL'. The second polariser used was polariser 'III', henceforth referenced as 'analyser' or 'ANA'.
The mentioned polarisers are Ti/Co supermirrors with 10 mm × 20 mm entrance and exit windows. The glass plates carrying the metal layers are slightly bent to prevent a direct transmission of neutrons without any reflections off the mirror. Unfortunately, exact values for the radius of curvature or the m-value are unknown.
In Fig. 3.2a the back end of the polariser can be seen, whereas Fig. 3.2b shows the corresponding neutron camera image from a CCD neutron camera.
The CCD (Charge Coupled Device) neutron camera in use was the *WAT-120N+ monochrome CCD camera* manufactured by *Watec*. To detect incident neutrons a scintillator inside the casing is used and resulting photon emissions can subsequently be detected by the camera. In the centre of Fig. 3.2b one can observe the different

layers of a polariser at the exit window. The light vertical traces are the positions where neutrons impacted, the dark areas in between show the positions of the neutron-absorbing cadmium layers. The random white dots in the image are thermal noise produced by the camera and are artefacts.

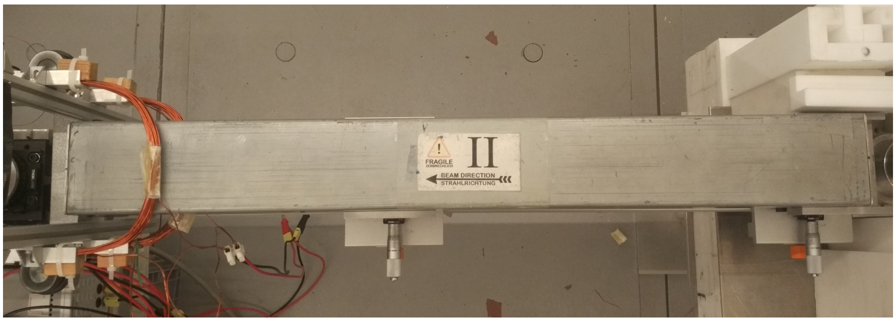

Fig. 3.1 – Image of polariser 'II'.

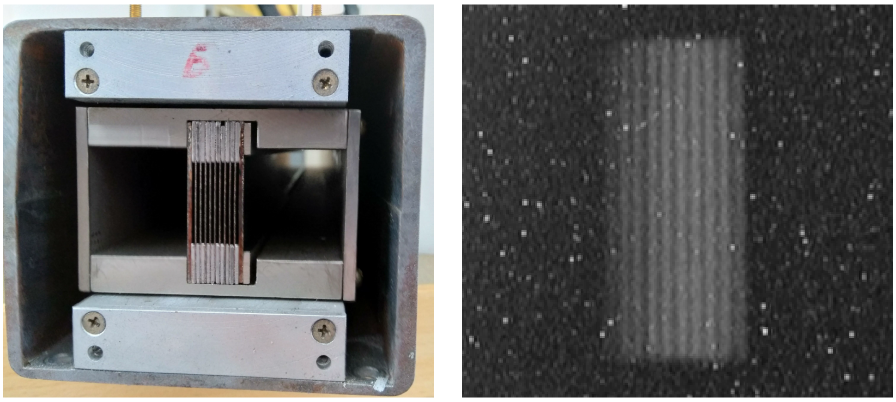

(a) Optical image. (b) CCD image.

Fig. 3.2 – Exit view of a polariser.

3.1.2 Helmholtz guide field (GF)

An ideal Helmholtz coil pair can be constructed of circular coils with radius R separated by a distance d, which equals the radius. The coils are supplied with equal currents so that the current flowing in the same direction in both of them produces a homogeneous field between the pair.

The guiding field used can be seen in Fig. 3.4. It is about 67 cm × 19 cm × 10 cm in size with 35 windings. Exact details about the guiding field could not be determined and so an experimental approach had to be taken. Measurements for the magnetic field strength at different currents were ascertained and can be seen in

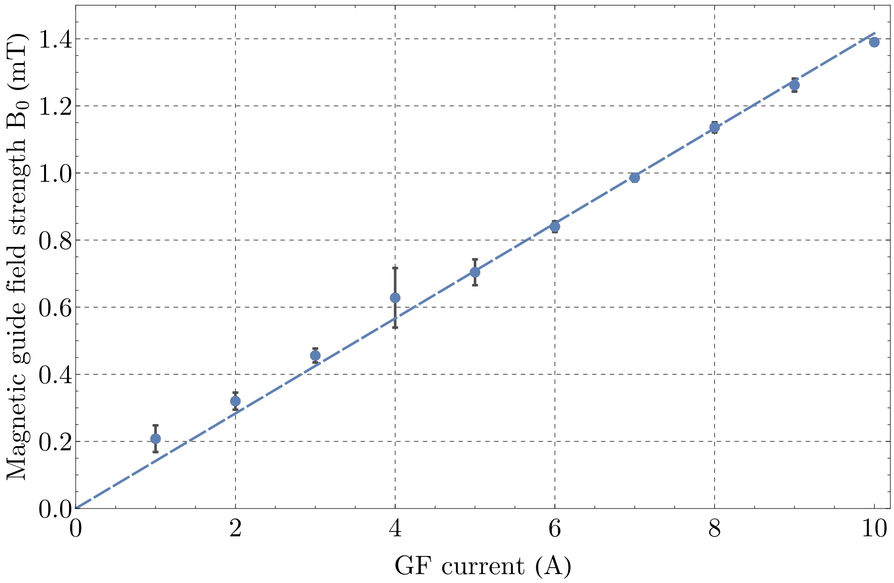

FIG. 3.3 – Characteristic curve showing the relation between the applied current and the produced magnetic guide field GF. The dashed line indicates a linear approximation ($y = 0.14\ x$).

TAB. 3.1 – Most important GF values.

GF current (A)	B_0 (mT)
0.5	0.21(4)
5.0	0.70(4)
10.0	1.30(1)

FIG. 3.3. The most important values for this thesis can be found in TAB. 3.1.

The guide field as well as the compensation field (CF) and the DC-coil flippers (SDs) were all supplied by a *HAMEG 4040* power supply using a General Purpose Interface Bus (GPIB) connection controlled by a manually written LABVIEW-program. The magnetic field was measured using a 3-axis hall teslameter (*THM 7025* by Metrolab Instruments SA) which exploits the effect that the Lorentz force causes a deflection of the charge carriers in a conductor perpendicular to the magnetic field and the current direction. This, in turn, leads to a charge separation, creating an electric field and thus, a voltage proportional to the magnetic field. This magnetic field strength can then be measured. For more details refer to E. H. Hall [45], or simply to W. Demtröder [46, p.94].

When using the GF heat development turned out to be a problem. The guiding field coils would become very hot when supplying the pair with currents above

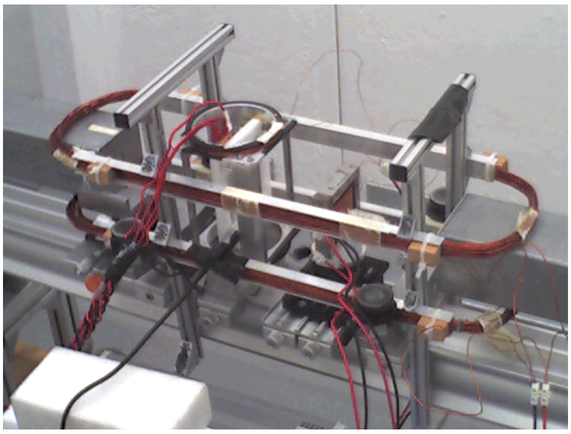

(a) Optical image.

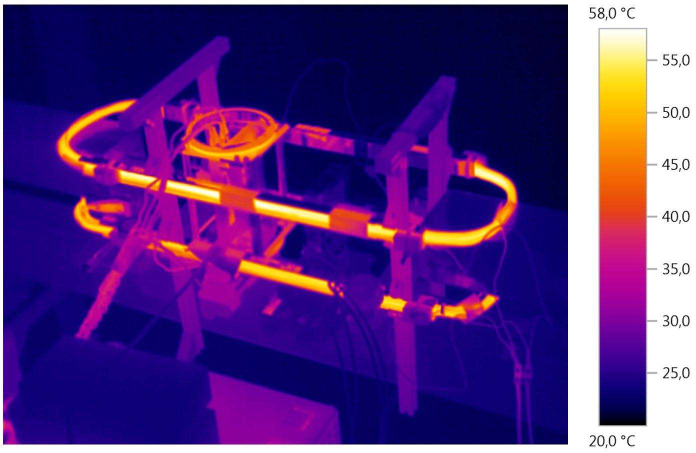

(b) IR image.

Fig. 3.4 – The guiding field under a current of 8 A (parallel). The coils for the compensation field of the current-sheet are still warm from a previous experiment.

5 A in a parallel setup. This limited the experimental possibilities somewhat since the magnitude of the guide field is important in selecting the wavelength of neutrons desired to flip by the DC-coil flippers in a resonator configuration.

3.1.3 Current-sheet (CS) and its compensation field (CF)

Current-sheet (CS)

The current-sheet in use was designed by R. Raab and consists of a 0.3 mm thick aluminium sheet with copper connectors and acts as a broad-band spin flipper [9, p.72]. As already mentioned in *Section* 2.4.1, the device relies on an extremely

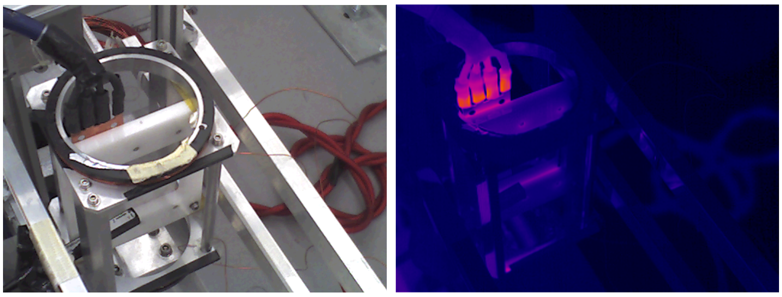

(a) Optical image. (b) IR image at 60 A.

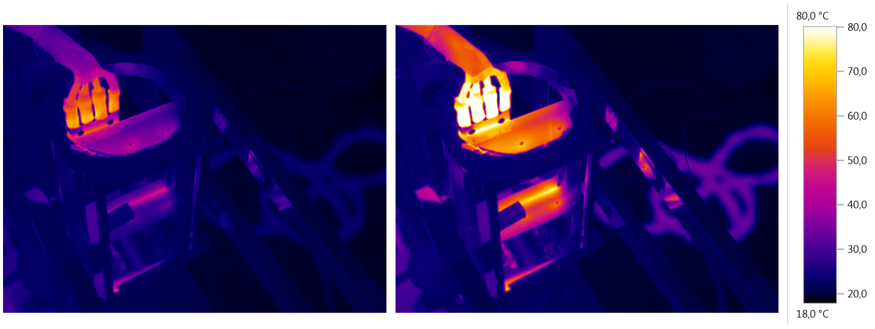

(c) IR image at 80 A. (d) IR image at 100 A.

FIG. 3.5 – The current-sheet under different currents.

non-adiabatic inversion of the magnetic field which can be achieved by the sheet, if the distance of the magnetic field inversion is small compared to the distance in which a neutron fulfils one Larmor rotation [10, p.6].

Originally, two of these CSs were designed for use on a 60 mm × 60 mm VCN beam. Since one of them (called 'New/2014' CS) was destroyed during the beam time at the ILL in 2014 [11, p.37], no experiments with this pair of current-sheets could be performed. This could have been interesting to compare the pair's spin flip probability and efficiencies. The relevant specifications for the remaining CS ('Old/2013') can be found in TAB. 3.2.

The CS can be used with currents of 100 A, although the benefit from strong currents subsides above around 50 A as at this point the current is high enough to align all neutrons to the magnetic field lines. Since this was the first time the current-sheet was used at the TWB, the old current cables were initially not available to use. Instead, four separate pairs of 3.5 mm copper cables were used with crimp receptacles on one side and were twisted together on the other end and plugged into the *TTi QPX600DP* power supply produced by *Aim-TTi* (henceforth referred to simply as *TTi*). Even though the cables were designed for currents up to 32 A it turned out that – due to their slightly different resistance – even at 45 A currents split between four cables, one pair began heating up much faster than any of the other ones. The plug around the power supply reached temperatures of up to 120 °C, which locally exceeds the maximum operational temperature of 70 °C by 70 %. The pair of cables that heated up reached temperatures of 86 °C (see Fig. 3.6).

To avoid any damage to the components, the cables were changed to 35 mm^2 copper wires originally intended as an audio cable set (*Dietz 20135*) which had previously been used to supply currents of 100 A to the CS [11, p.37]. They were already fitted with suitable crimp receptacles on one side. Since the cable came in two sets due to the previous feedthrough usage into an aluminium box of the Monopol experiment, *WGK 95F VP SW* adaptors by *Weidmüller* were used to connect the ends. This also provides a practical way to disconnect the cables in the future. Since the diameter of the cable was too large to fit into the small connectors of the *TTi* power supply, after consulting A. Pelczar from the in-house electronics workshop, the ends of the cables were manually split into four parts. One of the ends was used to be plugged into the power supply, the other three were twisted around the current-carrying end leaving about 50 mm for the plug. The copper connector still had a diameter of at least 6 mm^2, easily sufficient for the supply current of 50 A. The exposed copper wires were then secured with heat shrink tubes as insulator material. As expected, examinations with the infrared camera confirmed the resolution of the heat-up problems with the newly substituted cables.

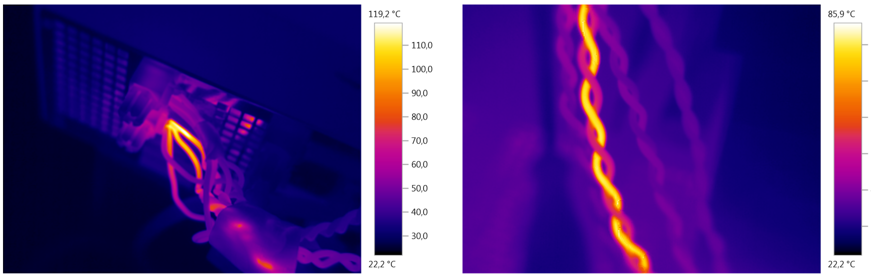

(a) Power supply connector.

(b) Cables leading to and from the CS. In front the overheating pair, in the background the other three pairs.

Fig. 3.6 – Infrared images of the current-carrying cables for the current-sheet at 45 A.

Compensation field (CF)

The compensation field of the CS was meant to be a Helmholtz configuration. As already described in *Section* 3.1.2 this would provide a homogeneous field in a broad part of the centre of the coils. However, the configuration is far from a Helmholtz

Tab. 3.2 – Specifications of the 'Old/2013' current-sheet [11, p.38].

Wire specifications	Isodraht Multogan 2000 MH G1 (DIN EN 60317-29)	
No. of windings (CF)	100	[47, p.11-15]
B_x	-34.127	$\mu\mathrm{T\,A^{-1}}$
B_y	-1.438	$\mu\mathrm{T\,A^{-1}}$
B_z	194.03	$\mu\mathrm{T\,A^{-1}}$
$\lvert B\rvert$	189	$\mu\mathrm{T\,A^{-1}}$
R_{CS}	0.28	Ω
$R_{\mathrm{CF\ coils}}$	1.16	Ω

coil pair and produces an inhomogeneous field documented by J. Bosina [11, p.37]. This made it difficult to measure accurate values for the field strength in the centre of the coils and to rely on these values to calculate the needed currents to compensate the guiding field. Once again, an experimental approach had to be taken in optimising measurements and determining when the applied currents were compensating the GF. These experiments will be described in *Chapter* 4.

In addition, as mentioned before, the CS as well as the CF were designed for use for very cold neutrons. However, to compensate even small guiding fields for thermal neutrons, much higher currents are needed for a thermal distribution of neutrons and so the experimental limits were soon reached.

3.1.4 DC-coil flippers (SD1 and SD2)[*]

Two identical DC-coil flippers were used during the experiments. The spin flipper itself consists of two coils, one producing a compensation field in the z-direction (SD#_CF), and a second field in y-direction (SD#_y) with the symbol # representing the respective coil flipper number. When adjusted correctly, the z-field can compensate the guiding field fully, producing a field-free area in the interior of the coil. An applied y-field then causes a Larmor precession of the neutron polarisation around the y-direction in the centre of the coil leading to a spin flip for certain wavelengths depending on the geometry as already outlined and described in Fig. 2.4.2.

The depth of the coils in the neutron's direction of flight (x-axis) was about 21 mm for the compensational field and around 17 mm for the inner (y-)field.

However, no documentation of the coils could be found, so, once again, an empirical-experimental approach was taken to determine the effects of the flippers on the beam.

A major difference to the theory was the additional magnetic iron joke around the

---

[*] Abbreviation 'SD' refers to its German term 'Spindreher'.

coils. New versions of the SD at the Atominstitut have aluminium structures for the copper coils. The difficulty was that it is not possible to measure the field strength of the internal magnetic field since this would have meant that the elements would have had to be disassembled entirely. An approach to calculate the field strength from the outside turned out to be unsuccessful, since the magnetic parts changed the characteristics. However, the functionality of the devices was never in doubt and the magnetic direction of the field on the outside could be determined by the usage of a simple magnaprobe when applying a current.
In Fig. 3.7 one of the used SDs can be seen.

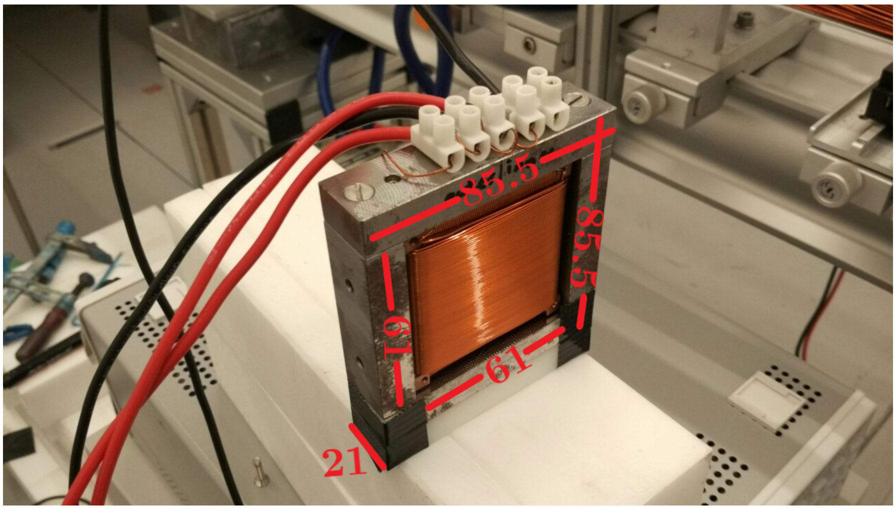

Fig. 3.7 – Front view of the SD2 DC-coil flipper used during the experiments. The dimensions of the component are given in mm.

3.1.5 Fermi-chopper

The Fermi-chopper that was used for all experiments can be seen in Fig. 3.8a and consists of several layers of aluminium and cadmium rotating with a frequency of 50 Hz and delivers two pulses per revolution due to the symmetry of the stack leading to a pulse repetition rate of 100 Hz. For the time-of-flight measurements each of the neutron packs was analysed by means of a Labview-controlled and FPGA-generated time-of-flight spectrum with 2 µs channel width.
The clocking of the chopper was supplied by the mains frequency of an ordinary power socket. It has to be mentioned that slight variations of the 50 Hz rotation frequency turned out to be quite noticeable not having been a relevant problem on the dichromatic beamlines previously. This issue was traced to the inconstant supply frequency and shifted the measured time-of-flight spectra somewhat. It was possible to eliminate this complication by considering the pulse frame rates of the chopper

and scaling the measurements to the mean frame rates of the Fermi-chopper, still causing some unknown uncertainties. On the long run, an electronically frequency-stabilised power supply for the instrument could be desirable.

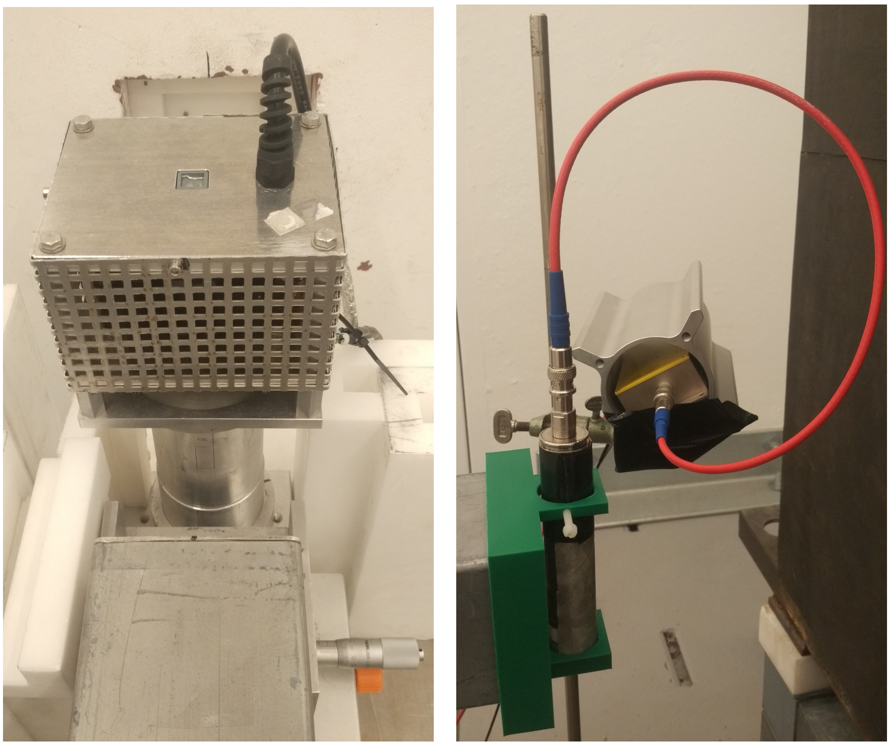

(a) The Fermi-chopper attached to the X95 carrier rail.

(b) The ^{3}He proportional tube with the preamplifier (yellow casing) attached to the supermirror with a 3D-printed mount (green).

Fig. 3.8 – Permanent instruments of the experimental setup.

3.1.6 ^{3}He neutron detector

The detector used for the TOF measurements was a ^{3}He proportional counter with an inner diameter of 21.2 mm under a pressure of 4 bar. It consists of a cylindrical cathode tube with an isolated wire placed in the tube centrally under a voltage of 760 V. For the experimental setup and its parameters the comparably small effective thickness of the detector caused inaccuracies for the TOF measurements of values around 0.5 % [12, p.73]. The principle properties and working mechanisms can be found in *Section* 2.6.3.

With a value of more than $10^6\,\mathrm{cm}^{-2}\,\mathrm{s}^{-1}$ [12, p.74] the integral flux of the thermal white neutron beam is higher than any other beamline at the Atominstitut. This high flux can easily reach the upper limit for such proportional counters that can lead to saturation losses of the detector due to its dead time.

These impacts can be limited by using the time-of-flight analysis method. Through the dispersion of the neutron packages not triggering events simultaneously as well as the considerably long periods in which the chopper is shut compared to its open position the number of incident neutrons impacting at the same time is reduced. In addition, all our measurements were conducted with at least one polariser at a time additionally cutting down on the number of neutrons by at least a factor of two.

Due to the Poisson distribution of the time intervals between two consecutive neutrons [48] the dead time can be calculated according to

$$n_{\mathrm{r}} = \frac{n_{\mathrm{m}}}{1 - n_{\mathrm{m}}\,\tau} \tag{3.1}$$

with n_{r} representing the real count rate, n_{m} the measured count rate, and τ the dead time of the detector [12, p.76].

During the first measurements it appeared that, nevertheless, a noticeable dip in the maximum of the neutron spectrum was visible attributed to mentioned detector saturation. This problem was limited first by adding a cadmium aperture after the chopper to decrease the number of impacting neutrons. Subsequently, after adding another supermirror further reducing the total flux to the detector, the issue was resolved and the cadmium apertures removed.

To be able to simply rotate the supermirrors without having to adjust the detector manually by moving it in front of the exit window on a separate stand Kasuma Obigane designed a 3D-printable detector mount for the polarisers (see FIG. 3.8b).

3.1.7 Measurement corrections

When using different instruments to measure neutrons on a polychromatic beamline a few relatable effects associated with the devices have to be taken into account, as shown by W. Mach [12, pp.70]:

Firstly, the chopper timing offset Δt comes into play because of the built-in photo sensor that delivers a TTL signal to register the start of a TOF measurement when the chopper opens. The sensor shows to have a constant offset of

$$\Delta t = 5.0851(1)\,\mathrm{ms} \quad [12, \text{p.73}]. \tag{3.2}$$

Secondly, the finite opening time interval of the chopper motivates the consideration of a chopper opening function $C(t)$. Mathematically speaking this leads to a convolution of its opening function with the neutron spectrum. However, this seems to be only a small correction. It turned out that the effective chopper func-

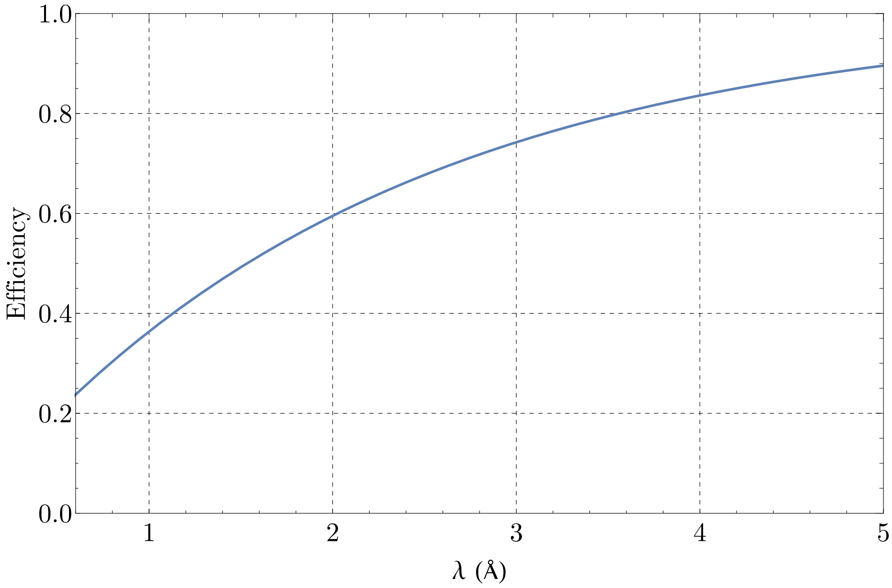

Fig. 3.9 – The efficiency of the ^{3}He detector for an active volume with an effective diameter of 21.2 mm at a gas pressure of 4 bar.

tion for the Fermi-chopper in use can be approximated excellently by a triangular function [12, p.73].
Thirdly, the detector efficiency and in this case the absorption cross section of ^{3}He in the proportional tube is – as mentioned in *Section* 2.6.3 – velocity dependent proportional to $1/v$.
Lastly, the absorption in air and aluminium traversed during the neutron's flight in the chopper can be taken into consideration, although this, too, only influences the measurements minorly [12, pp.72].

Since the chopper opens and closes depending on a time distribution and not instantly, the start and end time of the pulse is blurred and thus not well defined. The opening time t_{open} was determined to be

$$t_{\text{open}} = 0.2547(3)\,\text{ms} \quad [12, \text{p.73}]. \tag{3.3}$$

The efficiency of the ^{3}He detector can be found in Fig. 3.9. For shorter wavelengths the detection efficiency approaches zero and increases as the wavelength increases, eventually reaching a theoretical efficiency of 1. For neutrons in the thermal region with wavelengths of around 1.8 Å, or 25 meV, the efficiency is approximately 0.5. As pointed out by E. Jericha [49], it must be noted that W. Mach [44], who also computed the detector efficiency in his work, seems to have used the density of ^{4}He instead of ^{3}He for the calculations, making the detector seem significantly more

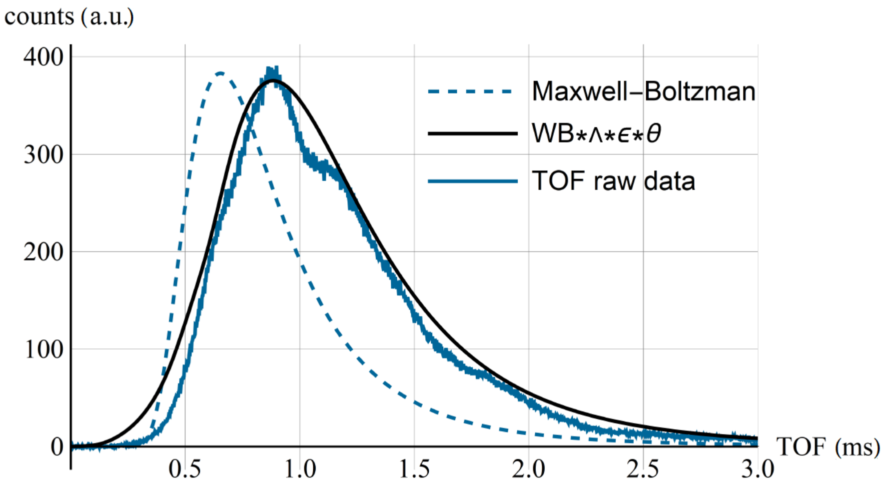

Fig. 3.10 – The theoretical Maxwell-Boltzmann distribution in comparison with the corrected spectrum and the corresponding raw data of a TOF measurement [12, p.77].

efficient for the observed wavelengths.

Fig. 3.10 demonstrates the experimental impact of the measurement compared with the theoretical TOF distribution. The corrected spectrum considers the white beam (WB) with the chopper opening function approximated by a triangular $\wedge$ function, the detector efficiency ϵ and the absorption Θ in the flight path. The influences for the chopper function as well as the absorption were rather negligible whereas corrections for the detector efficiency had a major impact on the measurements. The differences between the corrected and raw data measurements and the dips are very likely associated with the residual Bragg scattering of the sapphire/bismuth filters between the reactor and the experimental chamber [12, p.77].

3.2 Experimental configurations

The experimental configurations used in this thesis evolved and changed over the duration of the conducted experiments. The standard instruments always used were a Fermi-chopper mounted on an X95 carrier profile as well as a ^{3}He detector. Initially, just a single supermirror polariser (POL, marking ’II’) was placed in the centre of the collimated 20 mm × 20 mm white beam following the chopper. The neutron detector was then mounted to the exit window of the polariser and the spectrum of the white beam could be measured using the time-of-flight (TOF) method through the synchronisation of the chopper and the readout of the detector. In a second set of experiments, a second supermirror polariser, the so-called analyser (ANA, marking 'III') was placed in the beam behind the first one. This way, neutrons from the reactor would first pass the chopper, then the polariser and analyser and finally end up in the detector.

The third configuration additionally included a guiding field (GF) and a current-sheet (CS) with a Helmholtz coil pair as a compensation field (CF) between the polarisers. This setup provided a way to, in theory, invert the spin of all neutrons for all wavelengths. The analyser would then absorb all neutrons with an inverted spin.

The fourth set of experiments would then add a DC-coil flipper (SD1) that would invert the spin for a certain wavelength of the spectrum.

The fifth configuration added a second DC-coil flipper (SD2) instead of the current-sheet. When using both DC-coil flippers this would produce two separate flips for chosen wavelengths.

In the following chapters these different configurations will be described in detail. The chosen numbering will also be referred to in upcoming chapters.

3.2.1 Configuration 1: Polariser

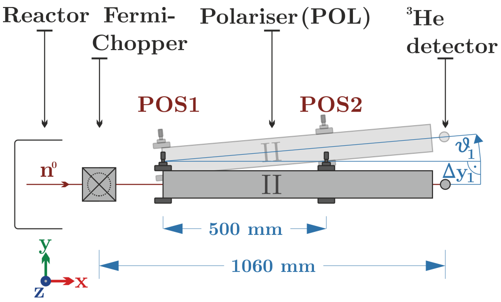

Fig. 3.11 – Configuration 1.

These first experiments were conducted together with W. Mach in June 2018. The initial configuration only used one polariser as seen in Fig. 3.11. The entire setup was mounted on a X95 carrier profile and adjusted using a laser alignment system. Neutrons coming from the reactor would be chopped up into small packages triggering the measurement start for the time-of-flight measurement of the spectrum. They would then penetrate the window of the polariser (POL) and through a series of total reflections for the (↑) spin direction and absorption for neutrons with an anti-parallel (↓) spin, as previously explained in *Section* 2.3.

Finally, the neutrons reached the detector at the exit window of the polariser where, upon impact the flight time of the neutrons would be recorded.

The laser adjustment helped to position the X95 carrier profile and subsequently chopper and polariser. To be able to move the position of the polariser in the ±y-direction two lateral linear translation stages with position indicators were fitted underneath the mounts. The one close to the reactor was labelled as POS1 and the polariser was positioned on it in such a way that its rotational axis lay exactly over the central position of the entrance window. The second mount position on the detector side was labelled POS2. From the parallel position determined by the laser adjustment the polarising mirror was then rotated to analyse the spectrum and its change since the mirror's reflectivity is both wavelength- and angle-dependent. Because of the simple configuration, no assertion on the degree of polarisation P could be made. However, the integral transmission and time-of-flight spectra could be analysed allowing a general understanding of the changes caused by the transmission of neutrons of the thermal spectrum in the polariser. These measurements were the first time a supermirror was used at a polychromatic neutron beam at the Atominstitut.

3.2.2 Configuration 2: Polariser and analyser

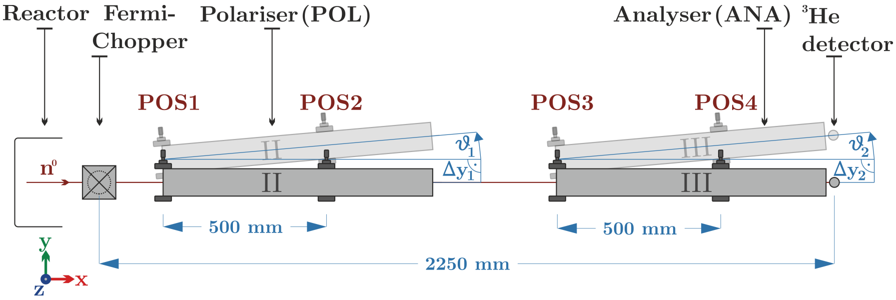

Fig. 3.12 – Configuration 2.

Previously, a single polariser was rotated around an angle ϑ_1. To perform experiments with these polarised neutrons, first one has to be able to analyse potential changes to the spectrum by adding another supermirror. Therefore, an analyser mirror was added to the setup, as can be seen in Fig. 3.12. The position of ANA was determined by its rotational angle ϑ_2 and its lateral displacement Δy_2 parallel to the incident neutron beam adding two additional degrees of freedom to the configuration. Again, linear translation stages were used to identify the initial position of the second supermirror with the help of the laser alignment system. Their respective positions were labelled POS3 on the reactor side, and POS4 on the detector side. Neutrons transmitted through the polariser would then traverse the analyser mirror, given the entrance window of the mirror coincided well with the beam direction of the polarised beam transmitted through the first mirror. The fact that, even in parallel position of the polariser, the transmitted beam would not exit the mirror parallel due to the internal geometry of the curved layers of the supermirror, caused some issues. This meant that the central position could not be calculated simply and an empirical approach was taken with the assistance of the neutron camera.

In perfect conditions, neutrons leaving the polariser would all be polarised in the (↑) direction. The traversing of the analyser should not change the spectrum because the polarised neutrons would all be transmitted, since the second supermirror also selects the (↑) spin.

This setup still did not allow for an analysis of the polarisation but again showed changes in the spectrum and the impact of rotating the mirrors. In addition, it became clear that a rotation of the supermirror made it nearly impossible to deduce the new impact position of the beam at the analyser's front window. An increase in the angle ϑ_1 would also additionally increase the angle at which the neutron beam exits the polariser because of its internal curvature. This essentially leads to an effective angle composed of the two mentioned ones. Therefore, defining a 'parallel' position was no longer practical since the precise beam direction after the polariser remained unknown. Instead the maximum integral transmission was selected as a reference. According to experiments conducted by A. Danner [50] the polarisation efficiency of the supermirrors should be high around the transmission maximum assuring that, as experiments advanced, the effects of components such as spin and DC-coil flippers would be clearly measurable.

3.2.3 Configuration 3: Polariser, current-sheet and analyser

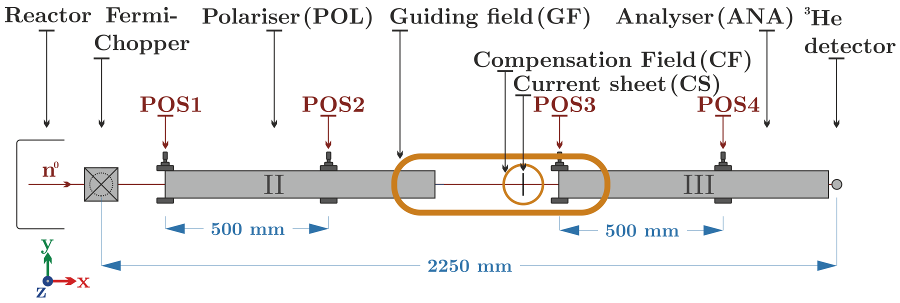

Fig. 3.13 – Configuration 3.

In this configuration, a current-sheet (CS) with a compensation field (CF) was added, as well as a guiding field (GF). This was the first time that spin flips could be produced. The purpose of the guiding field is to reduce the effect of outer magnetic field that may disturb the measurement. If the field is homogeneous it provides a simple and effective way to stabilise already polarised neutrons on the flight distance between the two polarising mirrors. As can be seen in Fig. 3.13 the guiding field was placed between the polarisers in such a way that neutrons exiting the polariser would already experience the homogeneous magnetic guide field. When the neutrons approach the current-sheet, the compensation field is set to annihilate the magnetic field in the centre of the coil pair and create a field-free area. The magnetic field of the current-sheet pointing in the ± y-directions then causes the neutrons to adjust their spins adiabatically following the field lines and fulfil a $\frac{\pi}{2}$ rotation around the axis of their flight direction (x-axis) also having aligned to the current-sheet's field pointing in the ± y-direction, depending on the direction of the current in the aluminium sheet. As previously explained in detail in *Section* 2.4.1, neutrons passing through the thin aluminium sheet are inverted due to the fast-changing field from the neutron's perspective.

In the resulting TOF-spectrum this would produce the dark field. Only neutrons that were not flipped or which ended up in intermediate states would then statistically give a probability to be transmitted through the analyser and appear in the spectrum. Experiments could then be conducted for different guide fields and compensation currents, for different CS fields. The angles of the polariser and analyser were not changed since they were already adjusted in the previous experiments to determine the positions of maximal integral transmission.

3.2.4 Configuration 4: Polariser, current-sheet, DC-coil flipper and analyser

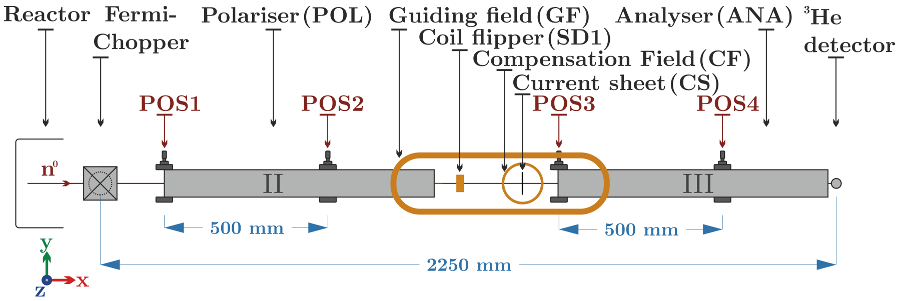

Fig. 3.14 – Configuration 4.

In the next characterisation step, a DC-coil flipper (SD1) was added in front of the current-sheet. These DC-coil flippers invert neutrons with one wavelength satisfying the resonance condition defined by the coil geometry and the magnetic field strength as given in Eq. (2.14). This configuration augmented the experimental possibilities since not only the effects of the different devices could be inspected separately but more importantly the efficiencies of each of the used manipulating elements (CS and SD1) as well as the spin flip probabilities.

3.2.5 Configuration 5: Polariser, two DC-coil flippers and analyser

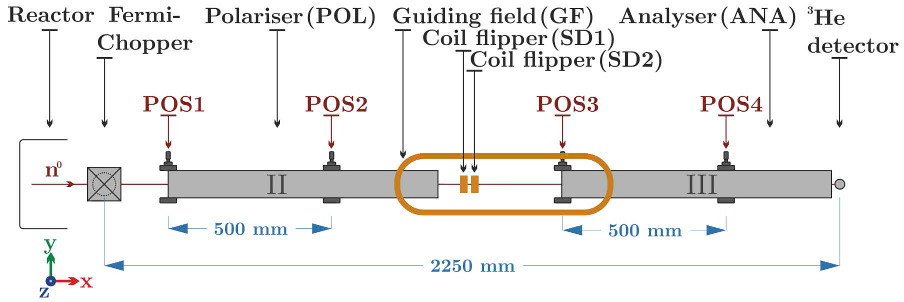

Fig. 3.15 – Configuration 5.

The final experimental setup was an alternative version of configuration 4. The current-sheet was replaced with a second DC-coil flipper (SD2) placed immediately after SD1. This, again, permitted to carry out experiments determining the efficiencies of the two flippers as well as the degree of polarisation.

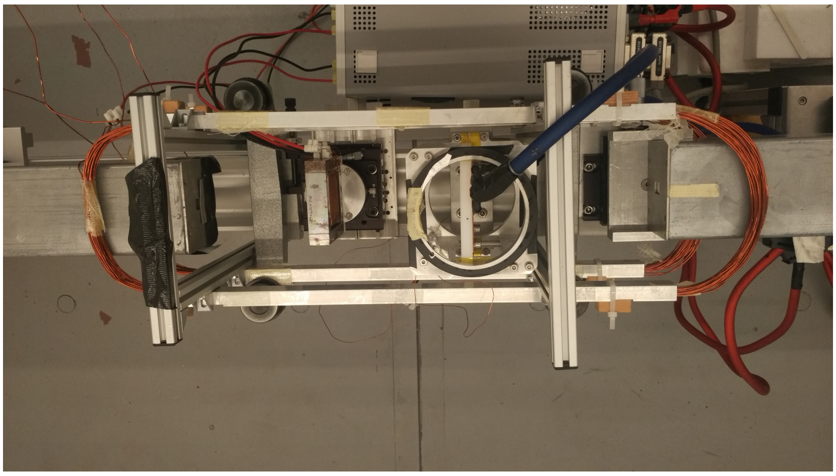

(a) Top view of the setup.

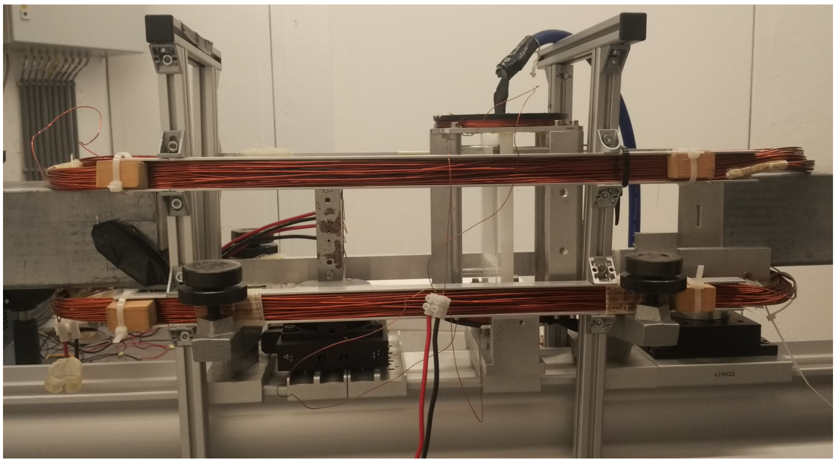

(b) Side view of the setup.

Fig. 3.16 – Images of configuration 4.

4 Measurements and Results

All of the following measurements concerning neutrons were conducted between June 2018 and January 2019 at the 'Thermal White Beam Facility' (TWB) of the Atominstitut. All shown data was corrected for wavelength-dependent detector efficiencies.

4.1 Configuration 1: Polariser

The first measurements using configuration 1 were set up together with W. Mach to gain a general insight on the impact of the polariser and how it changed the TOF spectrum.

Initially, it was not clear which direction the glass plates inside the two polarisers were bent. Through visual observations it could be determined that it was slightly curved to the left (anticlockwise) seen from the reactor side of the device. This assumption seemed to be verified soon after by according experiments observing the integral count rate at different angles ϑ_1. Several time-of-flight measurements were conducted to examine the modification of the spectrum since the transmitted neutron beam was expected to be dependent on the angle of incidence as well as the wavelength. The flight distance was determined to be 1.06 m.

The affiliated TOF spectra can be seen in Fig. 4.1a. The graph shows different time-of-flight spectra for various angles ϑ_1 of the polariser as well as a reference measurement without the supermirror in the beam. Plotting the intensity ratio of the neutron counts with the use of a polariser compared to without revealed the angle dependencies for different wavelengths, as can be seen in Fig. 4.1b.

In Fig. 4.2 the integral transmission of the supermirror POL as a function of its angle ϑ_1 relative to the neutron beam can be seen. The angle 0.0° represents the direction of the incident neutron beam. It shows that the transmission maximum lies around the angle of $\vartheta_1 = 0.27°$.

When normalising the measurements for the integral counts one can observe that the neutron spectrum gets colder with increased glancing angles (see Fig. 4.3). This is an expected result since higher polariser angles would less likely permit neutrons with higher energies to be transmitted. Faster neutrons have a smaller critical angle of total reflection making it more likely for them to be transmitted through the mirror material and have consequently a higher probability of being absorbed by the cadmium absorber plate cooling off the white spectrum.

The supposed beam direction is noted on the polarisers (see Fig. 3.2a) but it is not clear why the position would make any difference since the assumption was that the devices have a symmetrical build. Therefore some test measurements were conducted by placing the polariser in the beam in reverse.

The spectra at the mirrored glancing angles seemed to have lower intensities and the transmission of neutrons seemed to decrease especially for higher wavelengths. Since a thorough analysis did not seem necessary because of the higher neutron flux with the intended initial positioning in addition to the lack of extensive beam time it may be noted that such experiments could be of interest to improve the understanding of the polarisers.

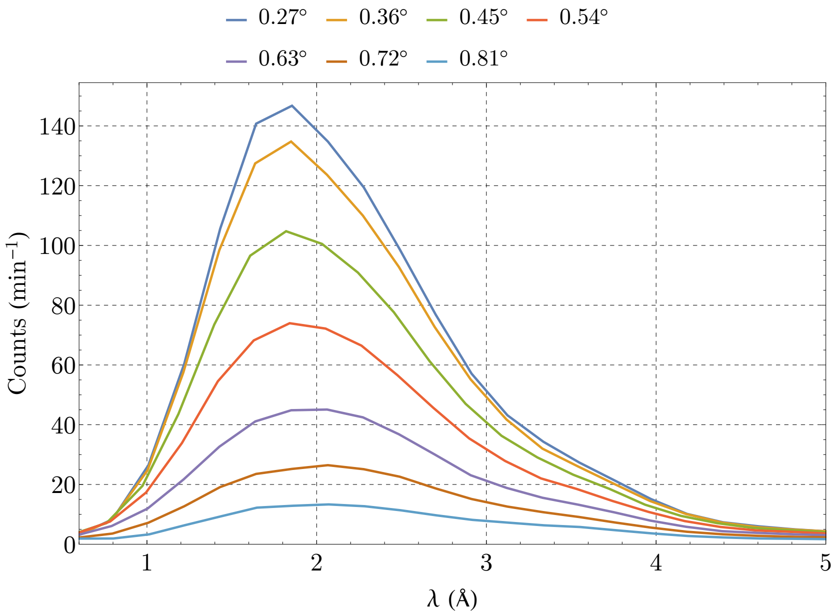

(a) The time-of-flight spectra for different angles ϑ_1 of the polariser.

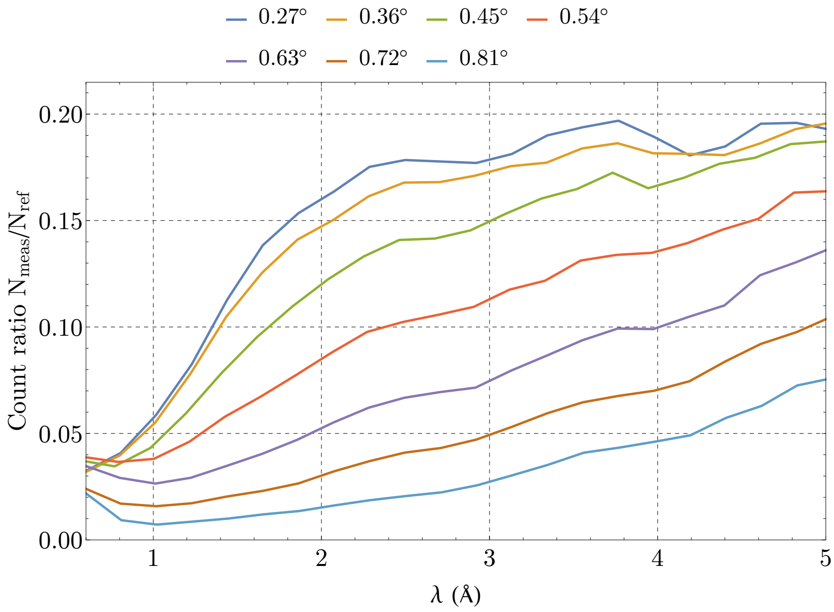

(b) Ratio plot of the time-of-flight measurements compared with a reference measurement without the polariser.

FIG. 4.1 – Changes in the spectra when rotating the polariser.

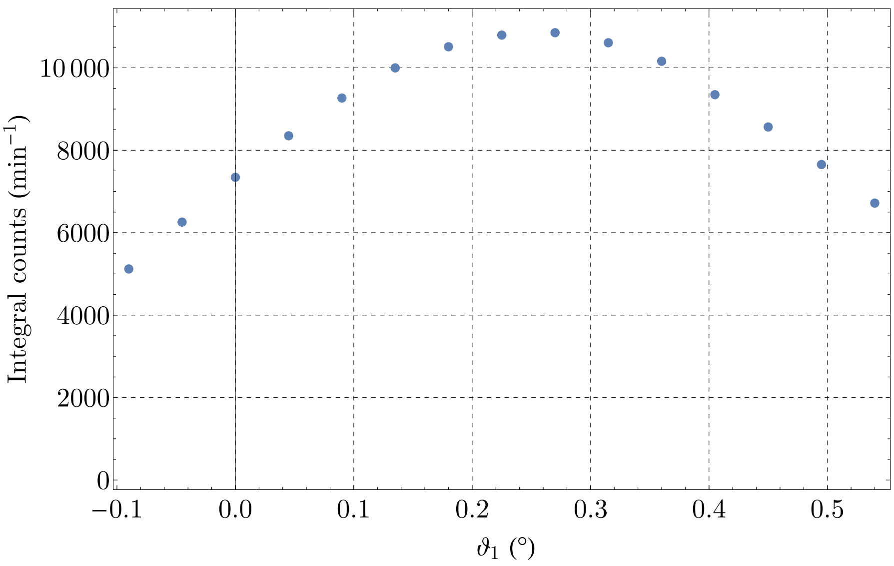

Fig. 4.2 – Integral counts for different angles.

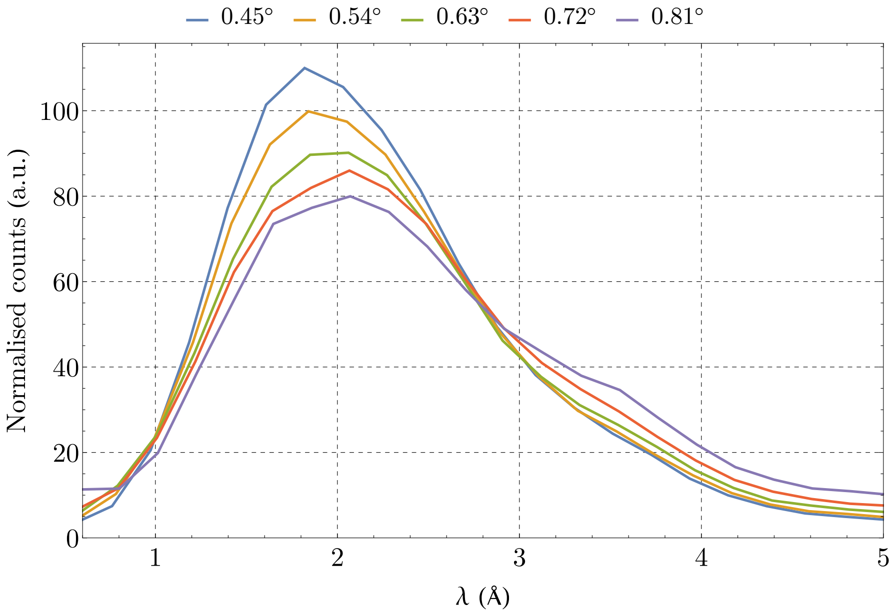

Fig. 4.3 – Normalised TOF measurements. The transmitted neutron spectra get colder as the angle ϑ_1 increases.

4.2 Configuration 2: Polariser and analyser

For this configuration the analyser was also placed in the beam fixed with two additional linear stages in the same distance as the stages on the polariser. This would permit for simpler referencing to rotational angles ϑ_1 of the first supermirror. The two new degrees of freedom for the second supermirror describing the position of the device were the angle of rotation ϑ_2 and the lateral displacement Δy_2. Aided by a laser adjustment system the parallel beam positions for the polariser and the analyser were measured and can be found in Tab. 4.1. The flight distance between the chopper and the ^{3}He detector was determined to be 2.25 m.

Tab. 4.1 – Parallel positions of the polariser and analyser.

Polariser POL		Analyser ANA	
POS1	POS2	POS3	POS4
10.5 mm	12.5 mm	12.5 mm	11.5 mm
$\Delta y_1 = 0\,\mathrm{mm}$		$\Delta y_2 = 0\,\mathrm{mm}$	
$\vartheta_1 = 0°$		$\vartheta_2 = 0°$	

Since the transmitted neutron beam from the polariser would not exit the supermirror parallely due to its internal curvature a new entry position for the analyser – parameterised as Δy_2 as the deviation from the parallel position – had to be determined. This, however, was only one of the two new degrees of freedom, that had now been added to the setup, the other being the angle ϑ_2 representing the rotation of the supermirror. Previously, only one degree of freedom ϑ_1 had been needed.

The first approach was to determine the original beam direction with the help of a neutron camera. At a distance of 0.475 m between POL and ANA, the position could be measured to be $\Delta y_2 = 5\,\mathrm{mm}$ (POS3 = 7.5 mm).

4.2.1 Rotation around the maximum transmission position

Keeping the polariser in the beam in its parallel position, the analyser was rotated around POS3 by adjusting POS4 resulting in a rough sweep for rotational angle steps between 0.12° and 0.23°. The best position was chosen to be POS3 = 7.5 mm and POS4 = 0.5 mm, although the integral maximum had been found at POS4 = 1.5 mm. This was due to the fact that the maximum polarisation would be not expected to be exactly at the maximum transmission position but slightly towards the direction of the internal curvature. Despite that, a high polarisation degree was still expected for any position close to the maximum transmission position.

It turned out that it would no longer be possible to determine the direction in which the polarised beam would traverse the analyser since the exit beam angle was unknown as well as the increase rate of the angle when additionally rotating the polariser. This lead to an approach where the beam entrance position of ANA was determined by the neutron camera and thereafter the maximum transmission angle was a reference position for further measurements.

4.2.2 Translatory movement of the analyser at maximum intensity angle

In the next step the previously chosen positions would provide a reference angle at $\vartheta_2 = 0.69^\circ$. A new sweep was conducted by keeping a constant angle and moving the analyser in a translatory motion in variation of Δy_2. The results can be seen in FIG. 4.4. As expected, the maximum transmission flux lies in the region of $\Delta y_2 = 5\,\text{mm}$ (POS3 = 7.5 mm) with a noticeable decrease in intensity as the supermirror position was moved 1 mm at a time.

TAB. 4.2 – Updated parameters of the polariser and analyser for configuration 2.

Polariser POL		Analyser ANA	
POS1	POS2	POS3	POS4
10.5 mm	12.5 mm	7.5 mm	0.5 mm
$\Delta y_1 = 0\,\text{mm}$ $\vartheta_1 = 0^\circ$		$\Delta y_2 = 5\,\text{mm}$ $\vartheta_2 = 0.69^\circ$	

It was concluded that – for the time being – the position of the analyser would remain at POS3 = 7.5 mm and POS4 = 0.5 mm corresponding to an angle of $\vartheta_2 = 0.69^\circ$ expecting that the polarisation degree would be above 90 % as well as maintaining a high neutron flux for statistical purposes and shorter measurement times. The new parameters can be found in TAB. 4.2.

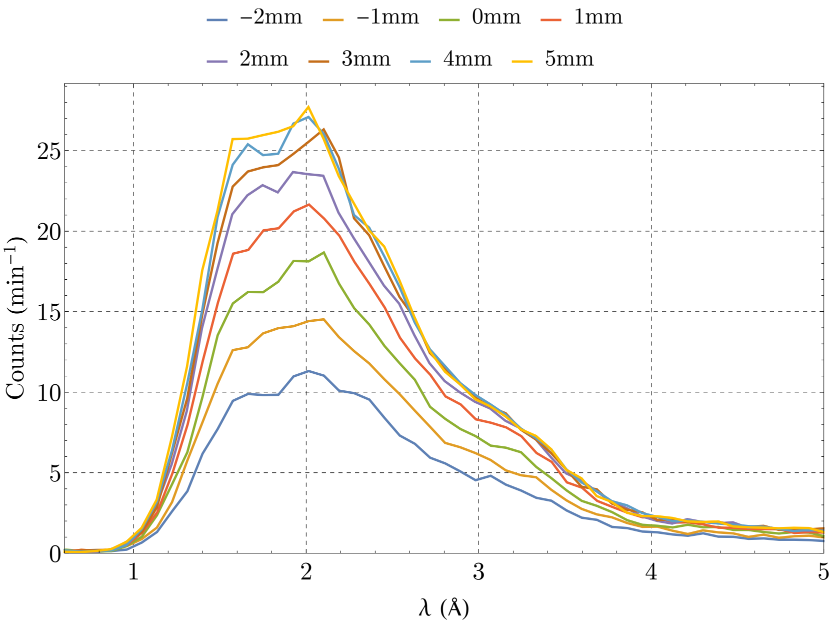

(a) TOF spectra for different values of Δy_2.

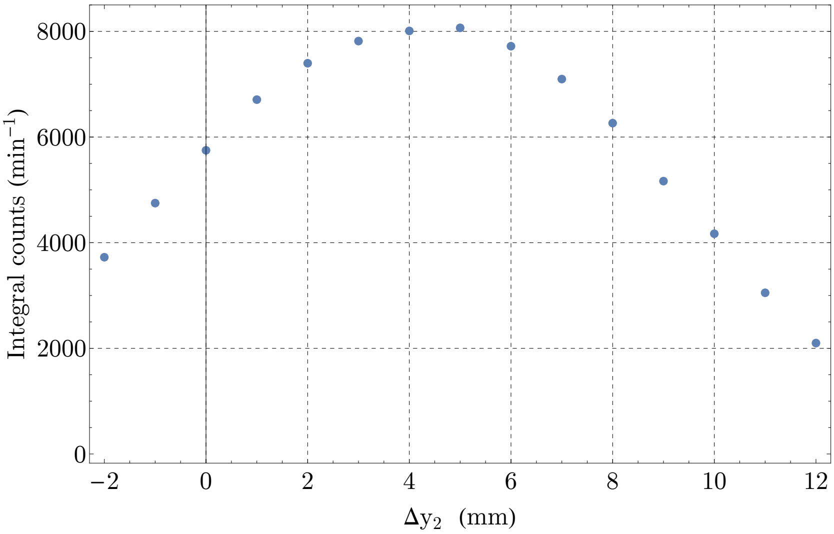

(b) Integral transmission for different values of Δy_2.

FIG. 4.4 – Changes in the measurements for translatory motions at a constant angle of $\vartheta_2 = 0.69°$.

4.3 Configuration 3: Polariser, current-sheet and analyser

In the next step the current-sheet (CS) with its compensation field (CF) was added to the setup as well as a guiding field.

4.3.1 Testing GF and compensation with CF

Until now, the guiding field (GF) with the role of stabilising the neutron spins to decrease the impact of external stray fields once they are polarised, was turned off. Setting a current of 10 A in parallel produced a magnetic field strength of 1.39(1) mT in the z-direction. This external field now had to be compensated by the compensation coils of the current-sheet (CF).

It had previously been found that the current-sheet was working well at currents of 50 A [11]. The CS current was set to 45 A since higher currents were not supported by the current-carrying cables thus far but the assumption was that this current would also suffice.

The results can be seen in Fig. 4.5 showing the effect of the current-sheet. A dip indicated a more effective spin flip (CS = 45 A).

The results illustrate that the most effective compensation current lies around 7.5 A. Following these measurements the coil temperatures of the magnetic fields

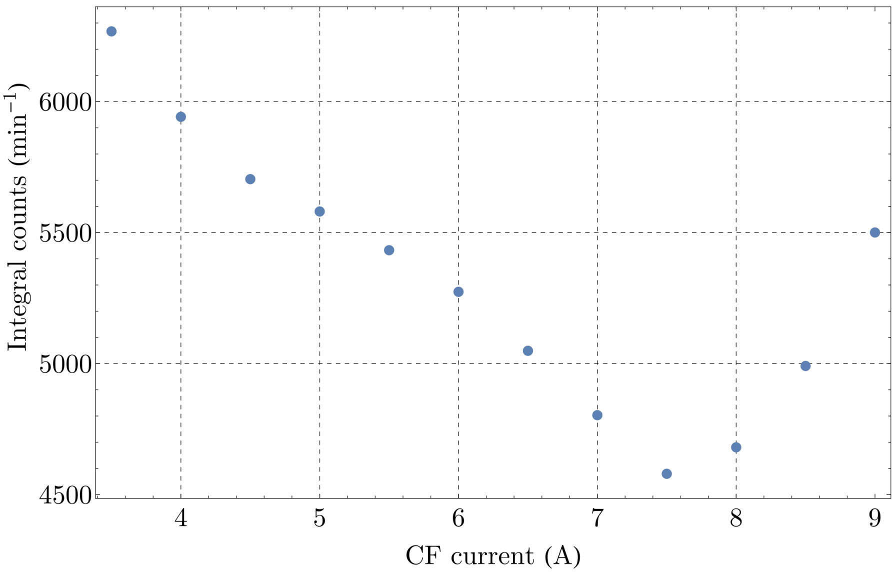

Fig. 4.5 – Integral counts in relation to the compensation field current for GF = 10 A and CS = 45 A.

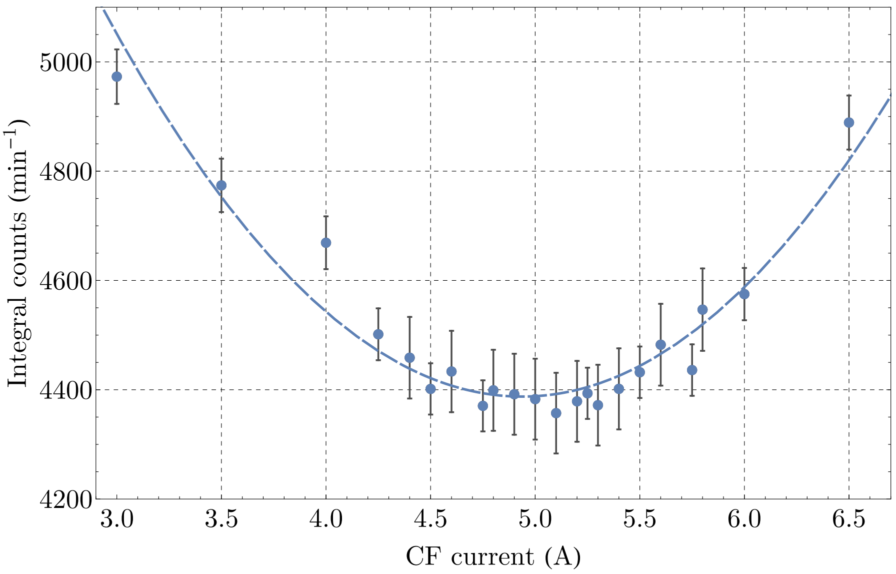

FIG. 4.6 – Integral counts plotted over the variation of the CF current at a constant GF current of 5 A and constant CS current of 45 A. The dashed line represents a quadratic approximation.

showed cause for concern and motivated the examinations with an infrared camera (see FIG. 3.4b). Thereafter the GF current was reduced due to the signs that the guiding field had not been constructed for such high constant currents.

The heat-up problems were solved by the choice of lower guiding field currents. Setting the current to 5 A in parallel produced a magnetic field strength of around 0.70(4) mT in the z-direction. The resulting measurements of the neutron transmission for different compensation currents can be seen in FIG. 4.6. The minimum of the integral neutron count was around a value of 5 A for the compensation field. This value cannot be entirely converted to a magnetic field strength since, as mentioned in *Section* 3.1.3, the compensation coils' geometry is nowhere near a Helmholtz configuration and produces rather curious and unknown fields depending on the current.
Nevertheless the compensation current CF could be localised sufficiently well.

4.3.2 Adjusting the rotational angle of ANA

The next step was to adjust the polariser POL to increase the efficiency since it was still positioned completely parallel to the beam. It was decided that the angle of rotation would first be set to $\vartheta_1 = 0.12°$. Henceforth, also the entrance position of the analyser ANA changed and with the help of the neutron camera it was located at POS3 = 1.5 mm with ANA now having been moved out of the direction of the beam through a translatory movement of $\Delta y_2 = 11\,\text{mm}$.

From Fig. 4.7 it can be deduced that the integral counts decrease strongly when rotating the analyser. The maximum integral transmission could be found at the same angle as for previous measurements with $\vartheta_1 = 0°$. The polarisation over the entire spectrum turned out to be rather constant with spin flip ratios between 2 and 2.5. This flip ratio was much lower than expected since flip ratios of up to 25 had previously been possible at the VCN beam at the ILL [11, p.58]. A spectral analysis of the TOF measurements was hence scheduled.
Because of the seeming consistency of the spin flip ratio over all angles the previously used angle of $\vartheta_2 = 0.69°$ was chosen for following experiments. The new parameters of the polarisers can be seen in Tab. 4.3.

Tab. 4.3 – Updated parameters of the polariser and analyser for configuration 3.

Polariser POL		Analyser ANA	
POS1	POS2	POS3	POS4
10.5 mm	10.5 mm	1.5 mm	−6.5 mm
$\Delta y_1 = 0\,\text{mm}$		$\Delta y_2 = 11\,\text{mm}$	
$\vartheta_1 = 0.12°$		$\vartheta_2 = 0.69°$	

The CS current was adjusted to 50 A because this had already been a satisfactory current during the beam time at the ILL and by this stage in the experimental phase the current-carrying cables had been updated. Due to the rotation and the increase in the CS current the CF current seemed to have shifted towards lower currents around 3 A (see Fig. 4.8).

To obtain a characteristic curve for the compensation currents for the most effective spin flip the guide field GF was changed in 0.5 A intervals from 0 – 5 A and for each of them the integral counts for currents between 0 A and the specific GF current was measured. This produced 10 plots similar to Fig. 4.8 with distinctive minima in the integral counts where the spin flip was most effective. These minima were then chosen as the compensational currents allowing to generate a characteristic plot indicating the relation between the GF and the CF currents at CS = 50 A (see Fig. 4.9).

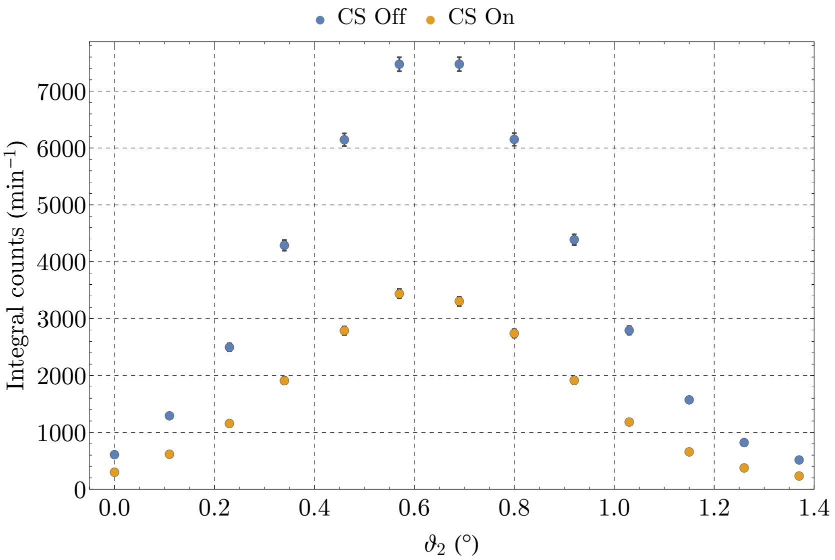

(a) Comparing the integral counts when the current-sheet was switched on and off.

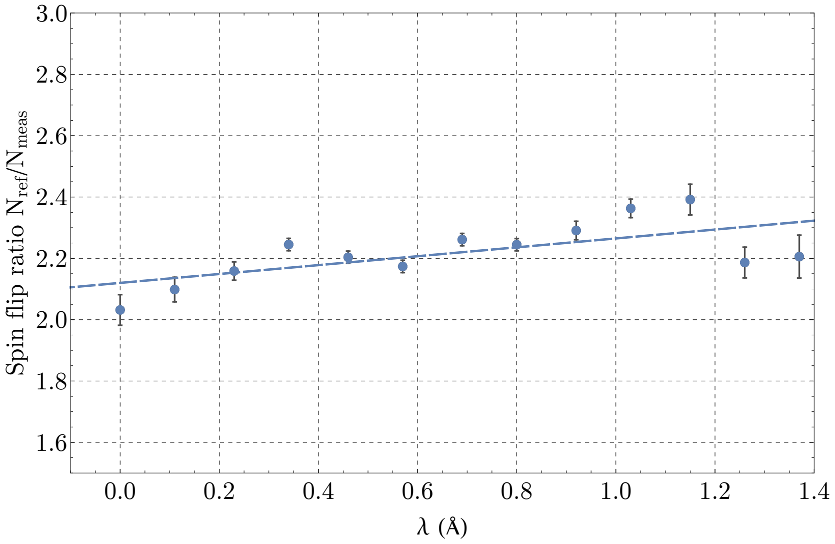

(b) Spin flip ratio plot to compare the effects of the current-sheet.

Fig. 4.7 – Experimenting with the effects of the current-sheet on the integral counts for a constant value of Δy_2=11 mm.

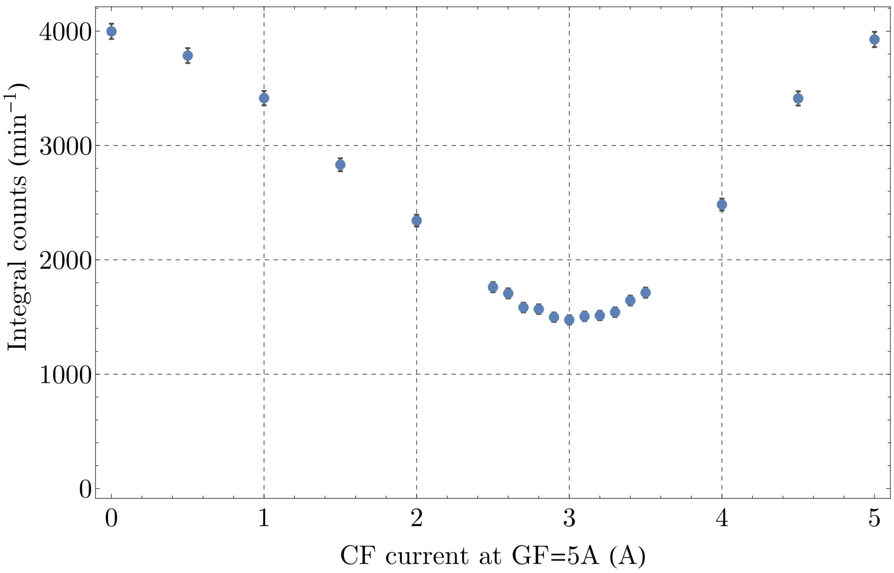

Fig. 4.8 – Integral counts over the CF current for GF = 5 A and CS = 50 A.

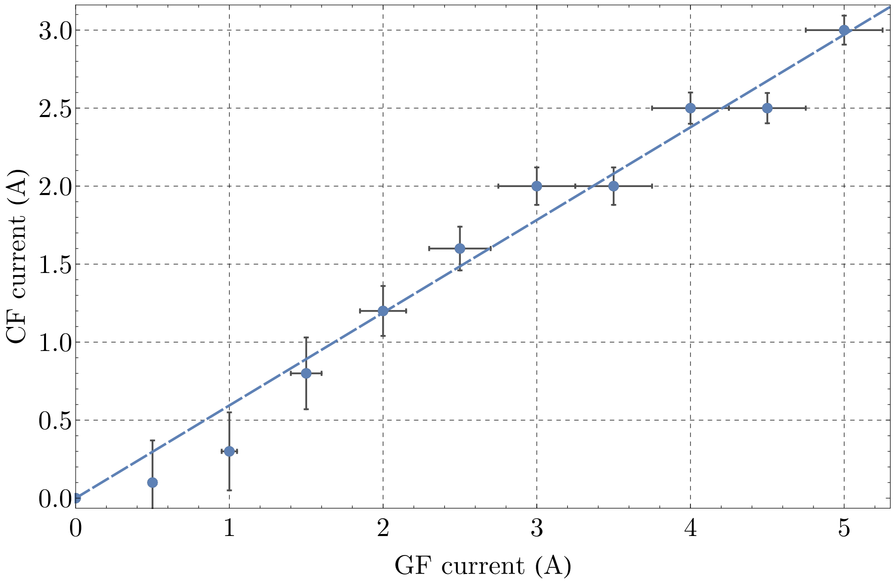

Fig. 4.9 – Relation between GF and CF. While error bars in the vertical direction are of statistical nature, the error bars in the horizontal axis originate from the limited resolving power due to a limited number of measurements and extrapolating the minimum values. The dashed line indicates a linear approximation ($y = 0.59\,x$).

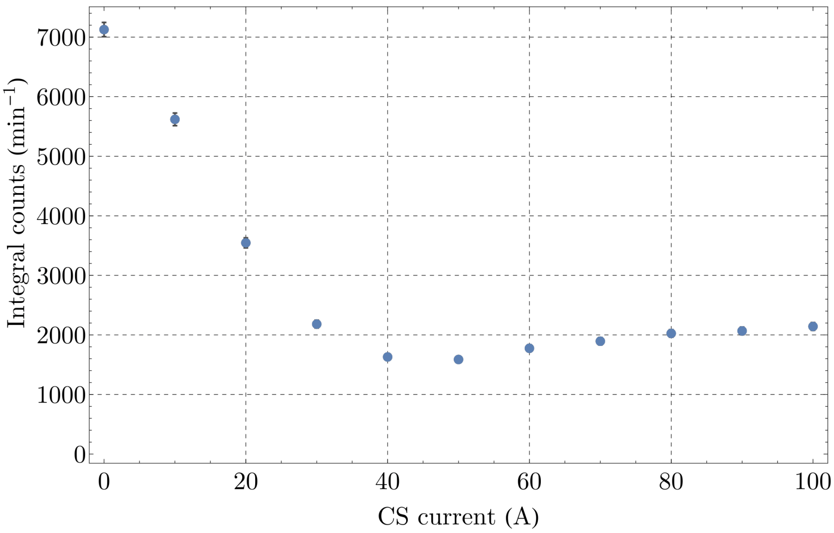

(a) Integral transmission for different CS currents.

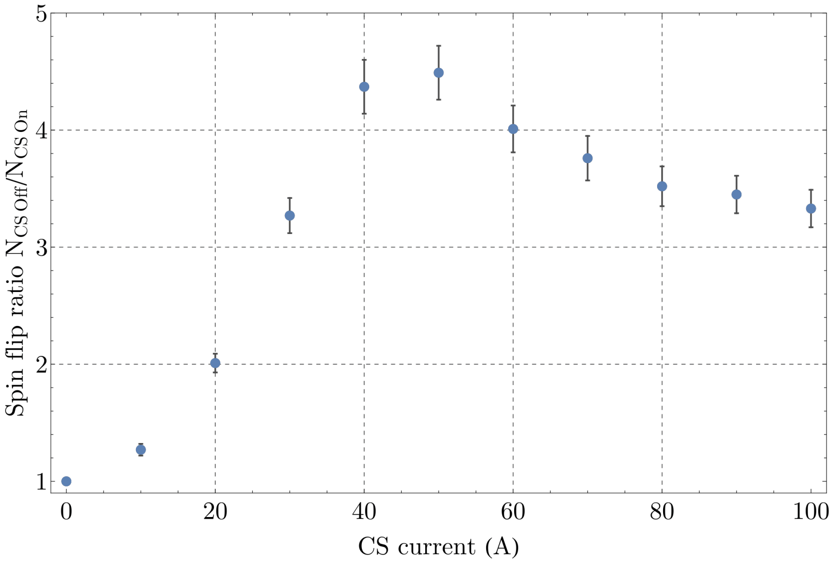

(b) Spin flip ratio in reference to CS = 0 A.

FIG. 4.10 – Effectiveness of the current-sheet for different currents.

4.3.3 Variation of CS currents

The previous uses of the current-sheet had shown that the best values for the direct currents of the CS should be around 50 A [11]. However, the measurements had been performed on a very cold neutron beam. To test the transmission rates for different currents, the polariser and analyser positions remained unchanged.

FIG. 4.10a shows the integral counts for different values of the current-sheet. A decrease demonstrates a more effective spin flip. The spin flip ratio plot in FIG. 4.10b are the measurements at a certain current divided by the reference measurement at 0 A. The measurements indicate that currents between 40 – 50 A produce the most effective spin flips. The increase in efficiency can be explained by the fundamental functionality of the current-sheet. If the spin is not exactly parallel to the magnetic field of the CS after passing it (y-direction), it will not be pointing into the negative y-direction afterwards indicating that a perfect (↓) state is not present which will result in a precession of the neutrons not exactly parallel to an exterior field and thus a deterioration of the spin flip efficiency.

4.3.4 Spectral spin flip ratio of the CS

So far, the transmission and spin flip ratio of the CS had only been observed integrally. This is only representative for the results with limitations since the spectral distribution plays a major role at the TWB. In theory, the current-sheet's efficiency should be independent of the neutrons' wavelengths. To test this, two sets of measurements were conducted: One with a guide field of 0.5 A and the according compensation current of 0.1 A, and another with a GF current of 5 A and a compensation current of 3 A, both with a CS current of 50 A.

The results can be seen in FIG. 4.11. The measurements show that for these different guide field and compensation field currents major differences in the spectral spin flip probability are visible. The most efficient wavelengths for GF = 0.5 A were between 2 – 3 Å whereas the GF = 5 A showed a maximum efficiency above 3 Å. Analysed spectrally, the peak spin flip ratio of 30 is very high for these specific wavelengths for the GF = 0.5 A. For GF = 5 A the maximum spin flip ratio can be found in the region of longer wavelengths.

These results are quite curious since no such outcome was expected. A stronger guide field would physically lead to a more stable spin state of the neutrons during their flight time in the field and should increase the efficiency. This was not the case. However, it is believed that the result was produced by the imperfections of the compensation field leading to the neutrons not fulfilling an adiabatic transfer into the y-axis exactly, subsequently not being perfectly orientated for the spin flip and therefore causing some kind of wavelength-dependent flip.

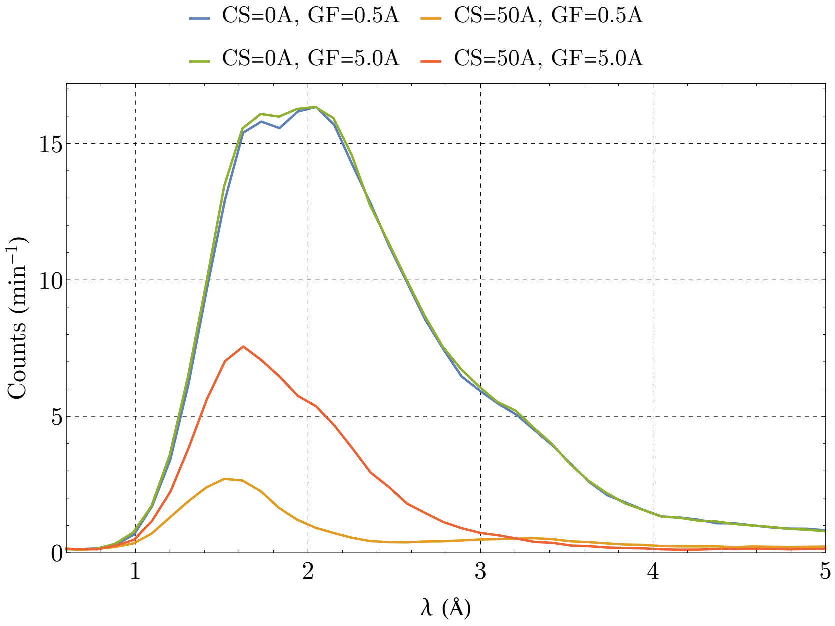

(a) TOF measurements for different settings.

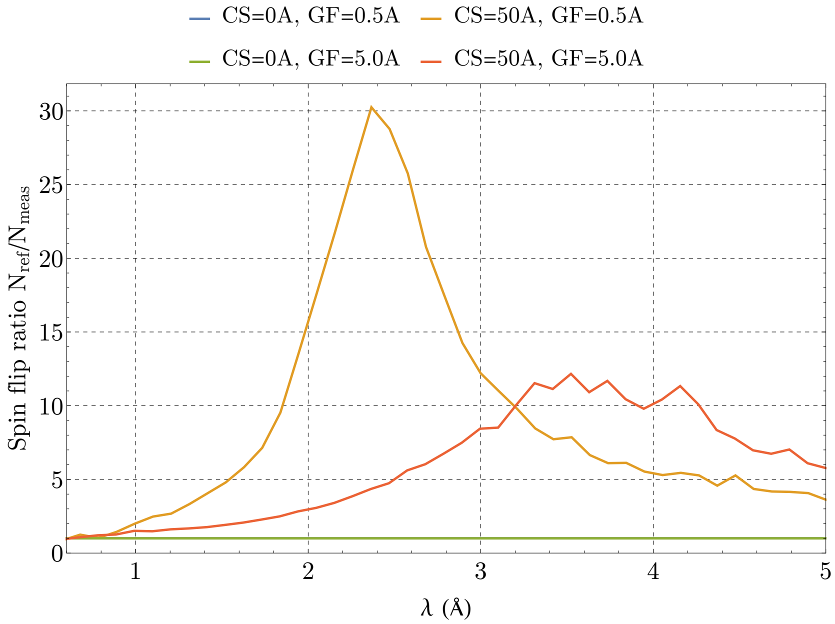

(b) Ratio of reference measurements with the CS turned off compared with the CS turned on to 50 A. In the graph, the blue line is hidden behind the green line, and obviously constant at a value of 1.

FIG. 4.11 – Spectral spin flip ratio of the current-sheet for different guide fields with compensation fields.

4.4 Configuration 4: Polariser, current-sheet, DC-coil flipper and analyser

The next step was to examine the DC-coil flipper SD1 in the polarised white beam. Its role would be to flip neutrons complying with the resonance condition.

4.4.1 Testing the DC-coil flipper SD1 without a GF

Since this experimental expansion also increased the setup by two degrees of freedom – the compensation field SD1_CF and the y-field SD1_y – the guide field was turned off completely.
Advances were made to simply perform a spin flip when setting a magnetic field in y-direction as this would ensure that the field truly was in y-direction with no component in z-direction caused by the guide field and imperfect compensation thereof.
To get a basic understand of the effect of the DC flippers, different y-field currents were applied as can be observed in Fig. 4.12. When applying currents of 0.2 A a fraction of the neutrons around the maximum seemed to be flipped. As the current increases more and more neutrons of higher energies are inverted causing an observable decrease in the count rate. The resonance condition is therefore met by more neutrons as it reaches wavelengths in which the maximum of the spectrum can be found. When observing the measurement with a current of 1 A, not only the resonance condition is met for wavelengths around 1.2 Å but also for neutrons with wavelengths around 4.1 Å. This is due to the fact that the applied current is so high it can flip neutrons of longer wavelengths twice when traversing the DC-coil flipper.
After some initial experiments, a y-field of 0.7 A was chosen as it seemed to flip neutrons in the maximum of the initial Maxwell-Boltzmann distribution which would increase the statistic significance when a spin flip was performed. The according magnetic field strength was again indeterminable because of the magnetic iron yoke around the set of coils and the geometry which did not permit to probe the central field. A dismantling of the DC-coil flipper would have been needed.
The resulting measurements can be seen in Fig. 4.13. A strong decrease in counts for wavelengths around 2 Å can be observed as well as a slightly less effective flip for wavelengths around 5 Å. The simple π flip condition seemed to be fulfilled at 2 Å and visible peak at 5 Å was attested to the 3π.
When increasing the y-field to 2 A, the resonance condition seemed to again be fulfilled for neutrons of 2 Å but in this case produced by the 3π resonance condition, with the π resonance flipping neutrons at higher energies of 1 Å. Additionally, the

field generated a dip at wavelengths around 3.5 Å and another at 5 Å – supposedly the respective 5π and 7π resonances.

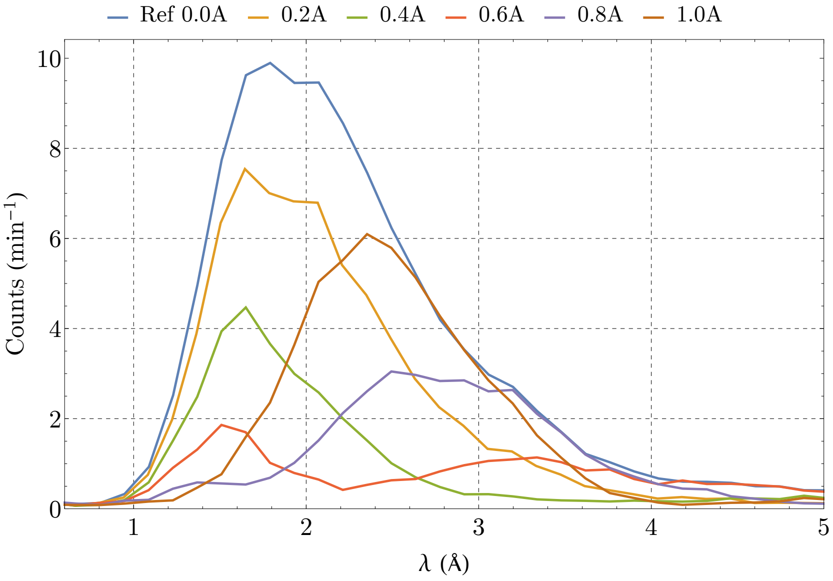

(a) TOF measurements for different SD1_y currents.

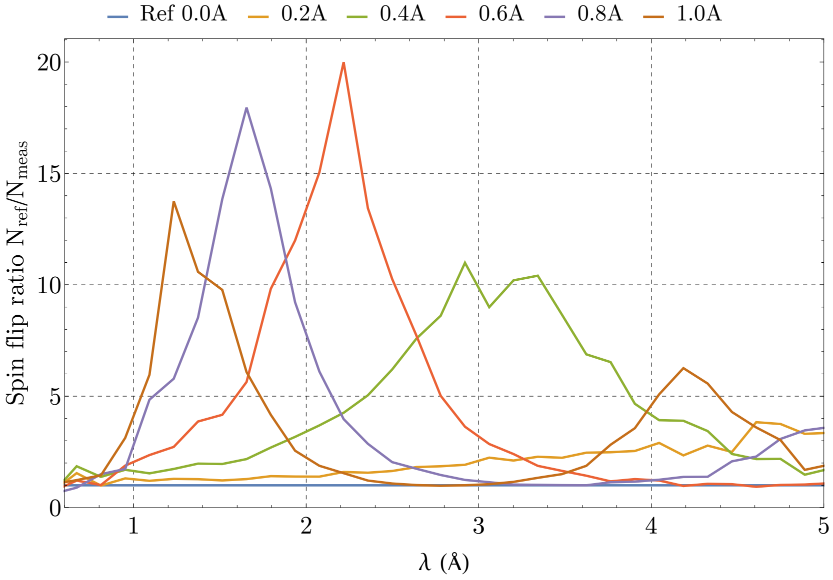

(b) Count ratio plot showing the effects of different SD1_y currents.

FIG. 4.12 – Variation of the SD1_y currents to determine which wavelengths would meet the resonance condition of the DC flipper.

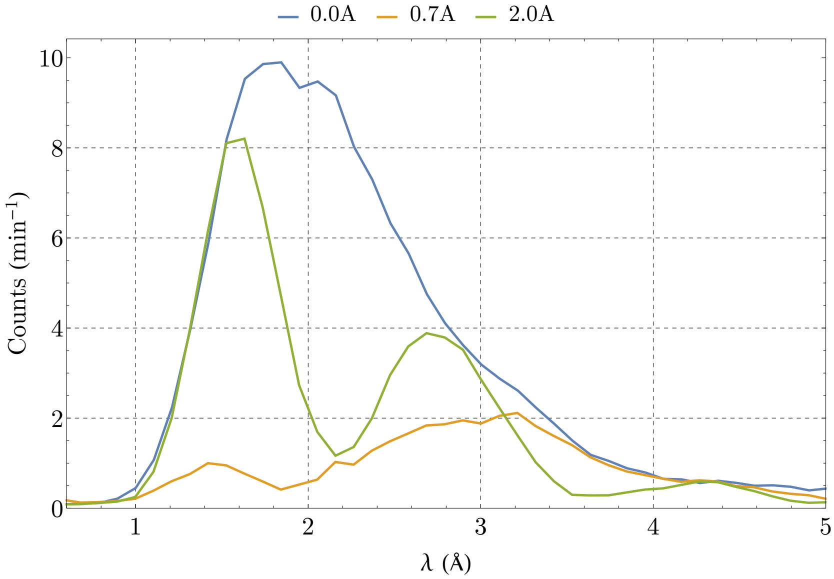

(a) TOF measurements for two different SD1_y currents.

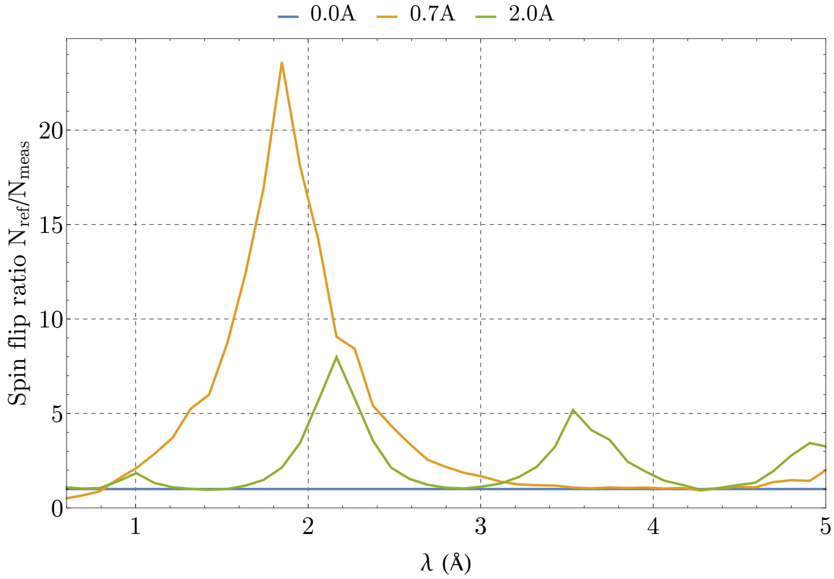

(b) The count ratio plot indicated that for a lower current one more effective spin flip in the observed spectrum is performed while for a higher currents less effective spin flips can be seen but for numerous wavelengths.

Fig. 4.13 – Demonstrating the effects of the SD1_y currents of 0.7 and 2 A compared to the initial spectrum.

4.4.2 Testing the DC-coil flipper SD1 with a GF

The guide field was set to 5 A (0.7 mT). When searching for a compensation field SD1_CF small currents were needed. The highest spin flip ratio for a SD1_y current of 0.7 A was located at 0.075 A, as can be seen in FIG. 4.14. At the resonance wavelength a spin flip ratio of up to 25 was reached, depending on the compensation current. Again, the magnetic field produced for the compensation field of the DC-coil flipper remained unknown for previously mentioned reasons. The resonance affected a broad range of the spectrum.

4.4.3 Current-sheet and DC-coil flipper

When using two spin manipulation devices on a polarised beam by performing four separate measurements, one can determine the efficiency of the two individual components as well as the degree of polarisation produced by the polariser. The approach is to conduct a measurement with both devices turned off (00), one of them on – (01) and (10) – and both of them turned on (11). As shown by EQ. (2.10) – EQ. (2.12) the efficiencies and the polarisation can then be deduced mathematically. For the white beam at the ATI, applying this method had never been done and therefore allowed for entirely new insight providing results that would show the efficiencies and the degree of polarisation of the entire spectrum and for all wavelengths.

The results obtained from measurements shown in *Section* 4.3.4 indicated that different guide fields would also provide for quite different efficiencies of the current-sheet at different wavelenghts. It was therefor decided – also because the guide field did not provide a noticeable efficiency increase as had previously been hoped – that the efficiency experiments would be conducted without a guiding field. This would simplify the experiments not having possibly unknown influences from the compensation field of the CS.

First, the four measurements were conducted using all iterations of CS = 0/50 A and SD1_y = 0/0.7 A. Results are shown in FIG. 4.15. From this the efficiencies of the current-sheet and the spin flipper could be calculated as well as the degree of polarisation. It can be observed, that both the current-sheet and the DC-coil flipper were quite successful at inverting the neutron spin for wavelengths around 2 Å with the current-sheet showing to flip a broader part of the spectrum while the DC-coil flipper had slightly more defined flip range. The spectrum with both devices turned on shows a shifted spectrum towards colder temperatures. Therefore only selected wavelengths were analysed for spin flip efficiency and polarisation, as can be seen in TAB. 4.4.

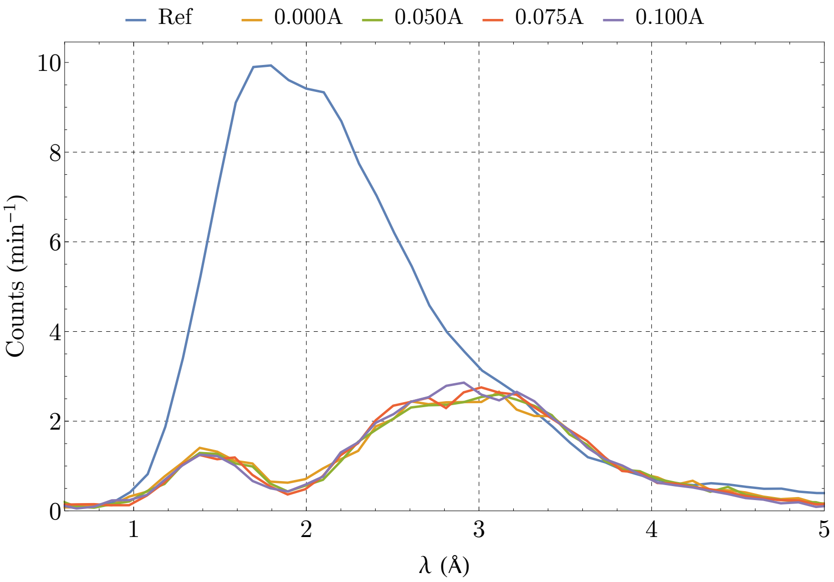

(a) TOF measurements for different SD1_CF currents.

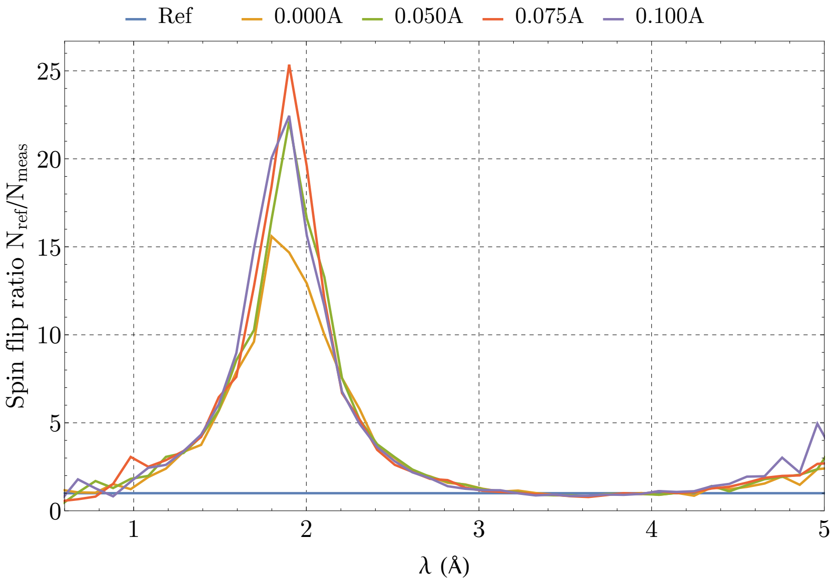

(b) Ratio plot for different SD1_CF currents. The highest spin flip ratio can be found for a SD1_y current of 0.075 A.

Fig. 4.14 – Compensating the GF = 5 A by varying the SD1_CF current at a constant SD1_y current of 0.7 A.

TAB. 4.4 – List of efficiencies of the current-sheet and the spin flipper as well as the polarisation degree for selected wavelengths for CS = 0/50 A and SD1_y = 0/0.7 A.

λ (Å)	e_{CS}	e_{SD1}	$P_P P_A$	$\sqrt{P_P P_A}$
1.84(5)	0.85(7)	0.81(7)	1.03(8)	1.02(4)
1.95(5)	0.98(8)	0.93(7)	0.90(7)	0.95(4)
2.05(5)	0.99(8)	1.00(8)	0.85(7)	0.92(4)

A similar measurement could be performed using a y-direction current of SD1_y = 2 A, where the 3π flip occurs in the maximum around 2 Å. The results can be seen in FIG. 4.16. Unlike in the previous example, the spin flip efficiency of the DC-coil flipper is successful in a much narrower region of the neutron spectrum and shows distinctive maxima and minima. As the wish was to perform a spin flip around the 2 Å region, the increase in the applied current caused a more localised spin flip with a higher resolution. In turn, this also caused additional minima at higher and lower wavelengths. In TAB. 4.5 one can find the calculated efficiencies and degree of polarisation for selected wavelengths.

TAB. 4.5 – List of efficiencies of the current-sheet and the spin flipper as well as the polarisation degree for selected wavelengths for CS = 0/50 A and SD1_y = 0/2 A.

λ (Å)	e_{CS}	e_{SD1}	$P_P P_A$	$\sqrt{P_P P_A}$
2.10(5)	0.67(10)	0.80(10)	1.05(11)	1.02(5)
2.22(5)	0.89(10)	1.00(11)	0.83(10)	0.91(5)

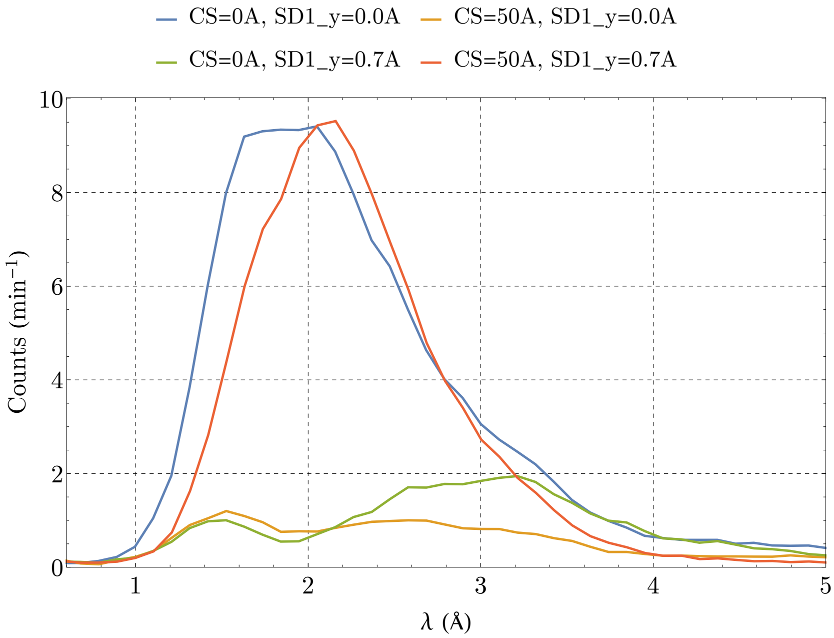

(a) TOF measurements to determine the efficiencies of the experimental devices.

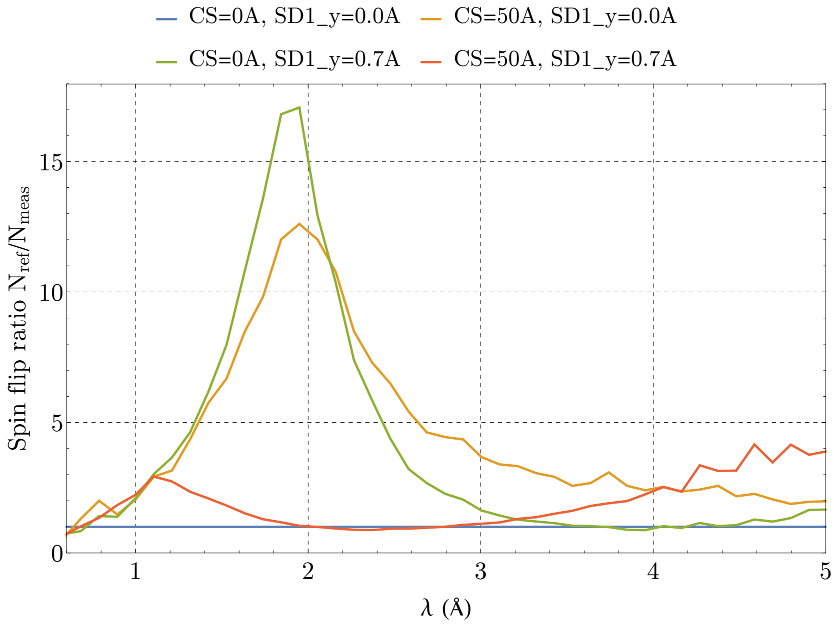

(b) Spin flip ratio plot resulting from the TOF measurements.

FIG. 4.15 – Measurements to determine the efficiencies of the experimental devices with CS = 0/50 A and SD1_y = 0/0.7 A.

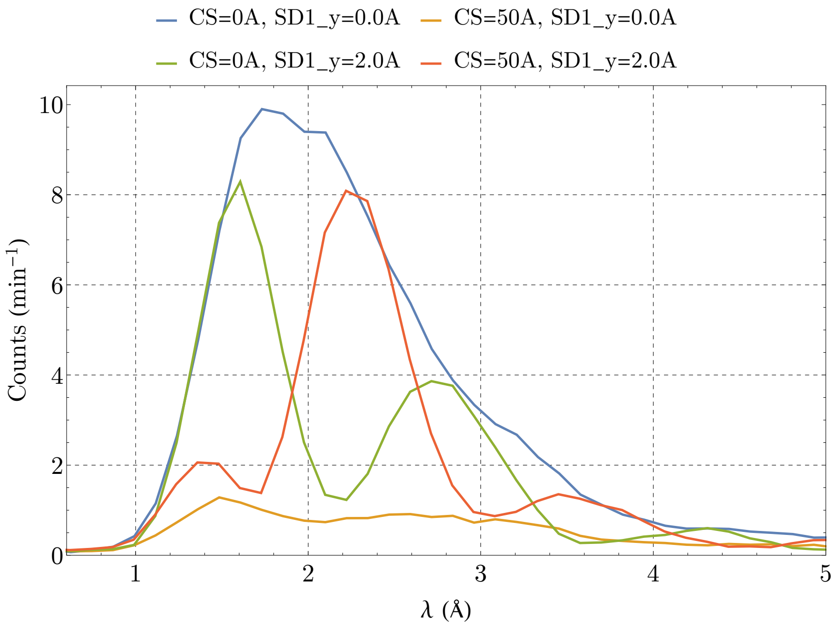

(a) TOF measurements to determine the efficiencies of the experimental devices.

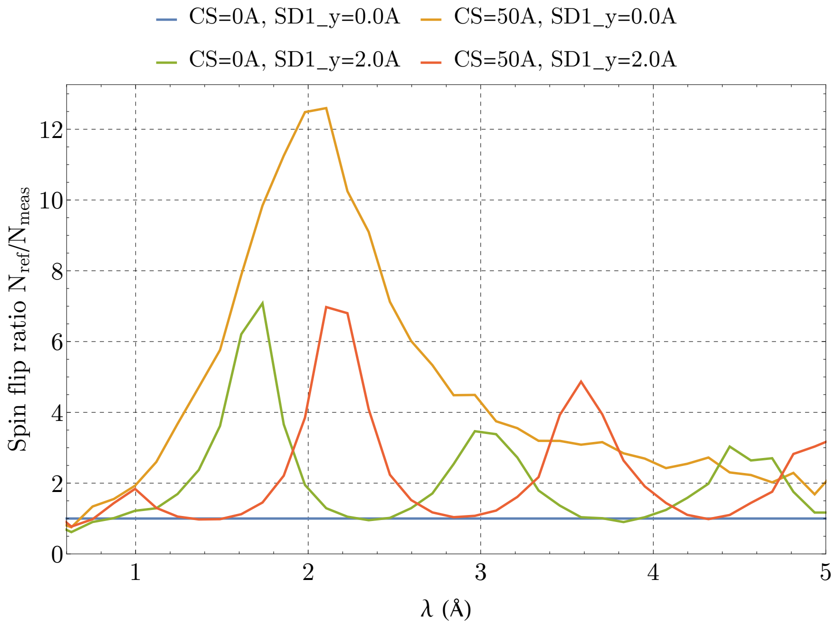

(b) Spin flip ratio plot resulting from the TOF measurements.

FIG. 4.16 – Measurements to determine the efficiencies of the experimental devices with CS = 0/50 A and SD1_y = 0/2 A.

4.5 Configuration 5: Polariser, two DC-coil flippers and analyser

In this section, the broad-band current-sheet was exchanged for a second DC-coil flipper of equal build, SD2. Initial experiments showed that the magnetic field produced by the second DC-coil flipper was in fact not equal in strength. Experiments – as shown before for SD1 – were conducted to determine the needed electric current where the inverting effect would occur at wavelengths around 2 Å. Having found such a spin flip for currents SD2_y = 1.0 A another polarisation efficiency experiment was initiated – again using Eq. (2.10) – Eq. (2.12).

The setup represents a simplistic version of the Monopol neutron resonator, with each of the DC-coil flippers simulating one individual coil of the resonator. For the used currents however, each coil produced a π flip, with two of these flips ideally resulting in a spectrum close to the non-manipulated one.

The results for the spin flippers and their efficiencies can be found in Fig. 4.17. The spin flip ratios are of a similar magnitude, as was expected. One can observe that the set currents of 0.7 A and 1.0 A did not perfectly match the same wavelength but were rather close with maxima around 1.8 Å and 1.6 Å, respectively. Despite optically being quite identical, the two DC-coil flippers did produce slightly different fields with SD2 showing a weaker spin flip ratio for the region around 3 Å and higher. The spectrum produced with both DC-coil flippers turned on seemed to interestingly be shifted towards slightly colder temperatures. The efficiencies and the degree of polarisation could be calculated for some selected wavelengths and can be seen in Tab. 4.6. It can be observed that for these measurements the efficiencies were overestimated by the calculations whereas the degree of polarisation was most likely underestimated, since the degree of polarisation would not have changed compared to *Section* 4.4.3.

Tab. 4.6 – List of efficiencies of the two DC-coil flippers as well as the polarisation degree for selected wavelengths for SD1_y = 0/0.7 A and SD2_y = 0/1.0 A.

λ (Å)	e_{CS}	e_{SD1}	$P_P P_A$	$\sqrt{P_P P_A}$
1.73(5)	1.02(13)	1.06(13)	0.78(10)	0.89(6)
1.84(5)	1.09(13)	1.10(14)	0.75(10)	0.87(5)
2.05(5)	1.11(16)	1.02(14)	0.68(10)	0.82(6)

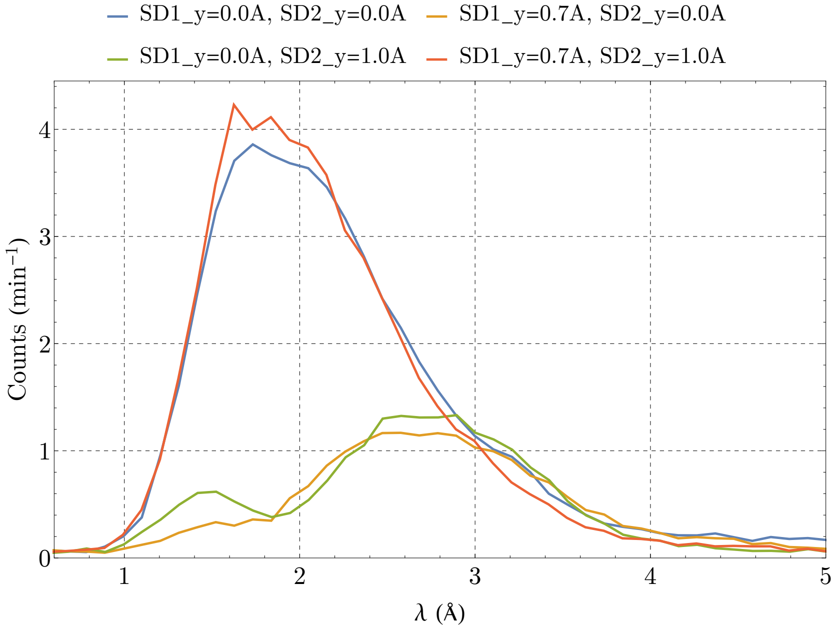

(a) TOF measurements to determine the efficiencies of the experimental devices.

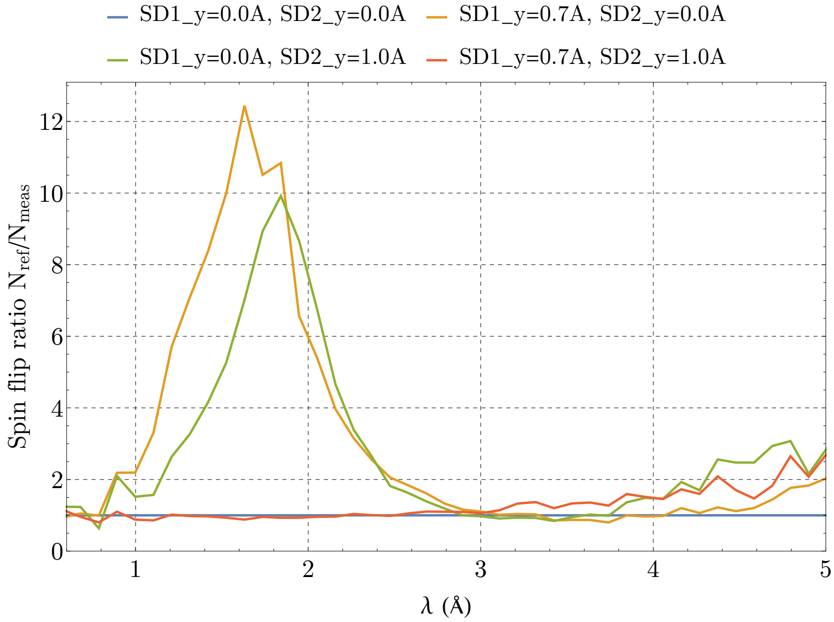

(b) Spin flip ratio plot resulting from the TOF measurements.

FIG. 4.17 – Measurements to determine the efficiencies of the experimental devices with SD1_y $= 0/0.7\,\mathrm{A}$ and SD2_y $= 0/1.0\,\mathrm{A}$.

5 Construction of MONOPOL

All of the measurements presented so far fulfil one main purpose: To path the way for MONOPOL at the 'Thermal White Beam Facility' (TWB). The final goal is to be able to demonstrate the full functionality and versatility of the resonator for thermal neutrons. Although the putting into operation of the new resonator was initially intended, the scale of the project would have simply been beyond the scope of this diploma thesis for time and workload reasons.

One of the tasks during this thesis was to drive the development of the MONOPOL resonator forward. The new version, MONOPOL 4.0, is characterised by some important improvements.

The entire electronics were redesigned by A. Pelczar and documented in two project theses ([51], [52]) to permit measurements with thermal neutrons. This induced major hardware changes to cater the needs of such electronic performance components and precise fundamental programming.

5.1 Power supplies

Thermal neutrons with velocities around $2200\,\mathrm{m\,s^{-1}}$ are much faster than VCNs which MONOPOL had previously been used with. This meant that, to induce a π flip for the same resonator length, higher magnetic field strengths, and thus currents, were needed. The power, however, increases proportionally to the square of the current. With currents of up to 25 A for each element this required effective solutions for the minimisation of heat build-up.

Also, the concept of the 'travelling wave mode' (TWM) relies on the idea that a pulse of neutrons travelling through the resonator is influenced by one single coil at a time. To ensure this, each of the 48 aluminium single coils should be timed precisely so that each one is only turned on in the very moment the neutron pulse traverses it and turns off as soon as the pulse has continued to the next coil now turning on the succeeding coil and so forth. This method, as mentioned in *Section* 2.7.1,

allows for a very high resolution but is limited by the ability to switch high currents with concise timing.
The two major problems mentioned above were solved by designing power supplies with a real and an artificial load (RL and AL, respectively). The real load would be a single aluminium coil of the resonator, the artificial load a dummy load with very similar electronic properties as the RL. With the aid of MOSFET-transistors the high currents can be switched between the two. Due to the high currents the stabilising time for the artificial load is of around 100 µs. A. Frank found that an intermediary period of around 600 ns during which the current flows on both the AL and the RL greatly improves the stabilising time for the RL in the process, reducing it to just a few microseconds [13, pp.23]. When powering up MONOPOL, after a short stabilisation period, the entire current will be guided over the AL per default only switching to the RL when needed. As such, the entire heat produced has to be dissipated via copper cooling elements as soon as MONOPOL has reached an 'idle' state ready for operation, not solely when the coils themselves are in use.

5.1.1 Cooling elements

To keep the sensitive electronics on the circuit boards from overheating, cooling elements with a water cooling system were designed by A. Pelczar and R. Gergen, manufactured externally and finalised in the mechanical workshop of the Atominstitut. In total, 60 sets of these elements, consisting of a cooling circuit element, a back-plate, two guiding pins and two pipe connectors were produced (see FIG. 5.1b). To connect the individual components, first a grinding of the connecting surfaces and subsequently, cleaning with ethanol was necessary. Afterwards, a soldering paste was used to connect the elements. The pattern applied can be seen in FIG. 5.1a. The elements were then cramped with foldback clips in order to assure sufficient pressure was applied during the baking. The assembled elements were then put into a *Thermo Scientific M 104* oven (manufactured by *Thermo Electron LED GmbH*) at 320 °C for 20 min and were then left to cool off with the help of an air fan.
Finally, the elements were polished on the surface to remove protruding stains the soldering may have left. This procedure was completed for optical gratification only.

To ensure that every single element was completely impervious, an air pressure test was performed. Three elements at a time were connected in series, put under a pressure of 4.5 bar and left pressurised under water for about 5 min. Air bubbles coming from the cooling elements would quickly show any leakage. FIG. 5.2a shows the test setup.
Of the soldered elements, 51 of the 60 were leak-proof the first time they were tested. The other elements seemed to leak especially in the areas where the guiding

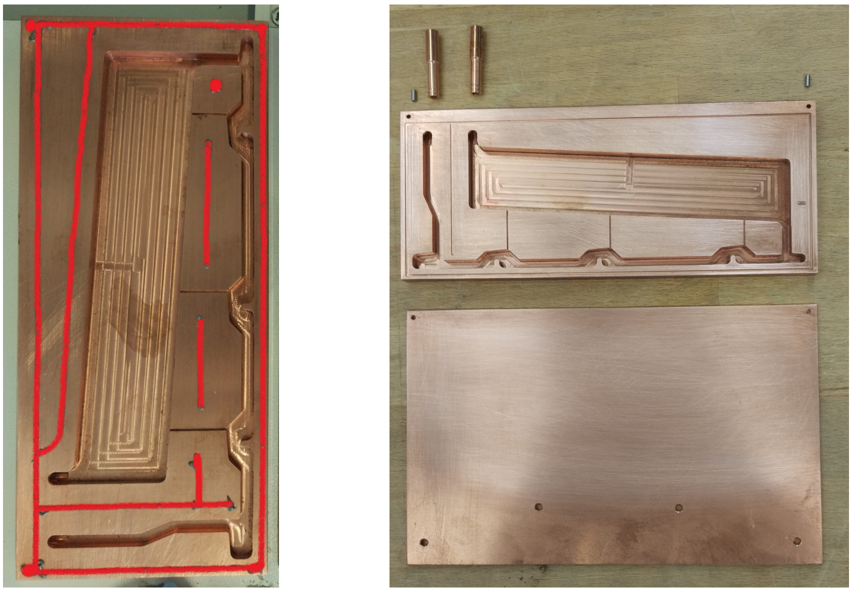

(a) Soldering pattern used (red).

(b) Individual components.

Fig. 5.1 – A cooling element before assembly.

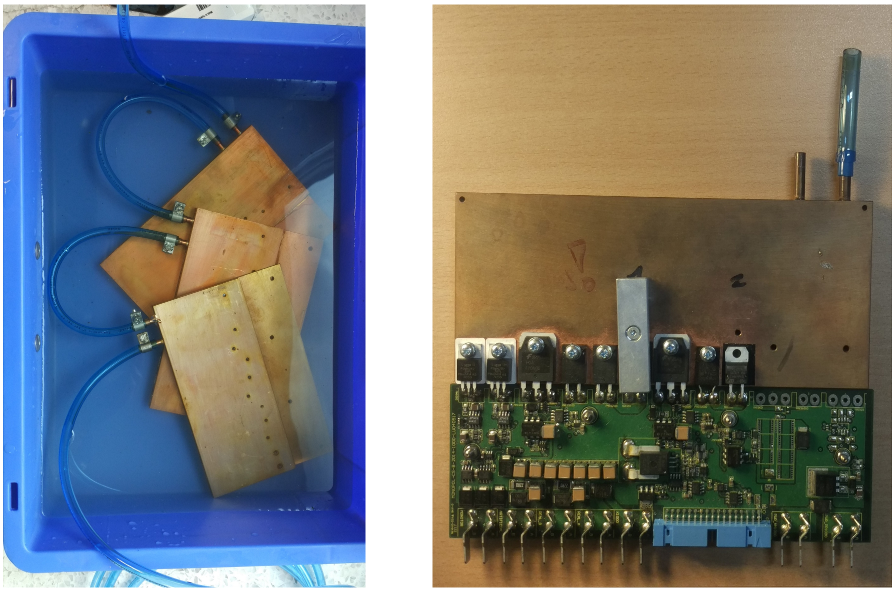

(a) Test setup for pressure tests conducted with a pressure of 4.5 bar in a water bath.

(b) A cooling element after assembly fitted with a power supply printed circuit board (PCB).

Fig. 5.2 – Cooling elements after soldering and assembly.

pins connected the circuit element to the back-plate. The reason showed to be that the pins did not always fit smoothly into the designated holes causing wedging which in turn produced unwanted gaps and subsequently leakage.
To fix this problem, extra soldering paste was applied externally to seal the elements and they were placed into the oven a second time (Label: 2x Ofen). One even a to be soldered a third time (Label: 3x Ofen). The pressure test confirmed the success of the measures taken.
After the pressure tests, all components were handed over to the in-house electrical workshop to be fitted with the power circuit boards and the appropriate power components. A finished element ready for use can be seen in FIG. 5.2b.

5.2 Testing of the electronics

To test the electronic components and to ensure that communication via the serial computer bus I^2C (Inter-Integrated Circuit) was possible, as designed, an assessment of the existing components was carried out.
In the new electronics design, when setting the desired values for MONOPOL using the graphical user interface on a computer, the signal is sent to the microcontrollers on the control board. Thereafter, the values are passed on to the backplanes and finally to the power PCBs.

With A. Frank, who had been responsible for the programming of the circuit boards, the initial testing of the control board, the backplanes and the power supplies were conducted (see FIG. 5.3).

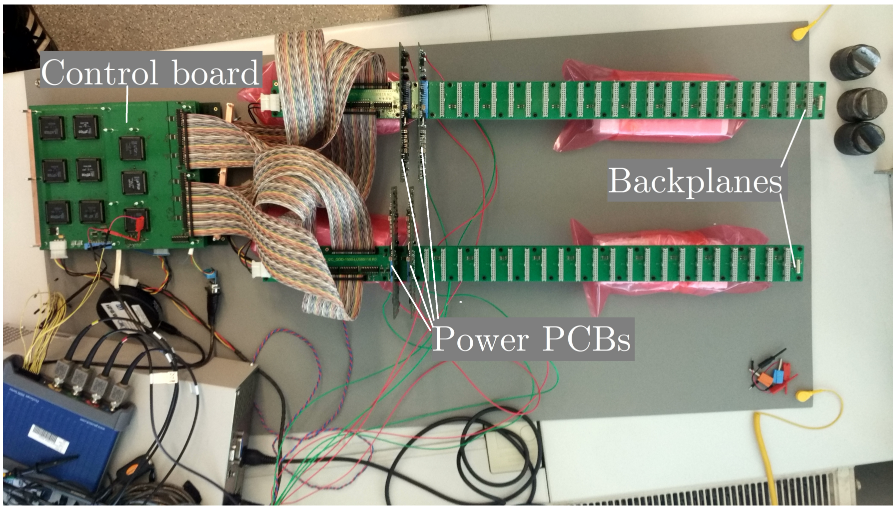

FIG. 5.3 – Experimental setup of the two backplanes with four PCBs.

The tests performed initially posed some problems and it seemed that a resistor in one of the backplanes had not been soldered correctly. After a thorough examination by members of the electronic workshop this issue could be resolved and both backplanes as well as the control board could be tested successfully and it was possible to establish I^{2}C communications with each of the 48 backplane positions. For information on the programming and communications of the setup refer to A. Frank [13].

5.3 Main Switch-Mode Power Supply (SMPS)

MONOPOL is in need of a direct current of 25 A at 12 V to supply each of the 48 individual coils. This results in a maximum power of 14.4 kW if one neglects the low supply power requirements for the main board and the control elements.

Therefore, three SMPS of the model *GKD(M).(H) 12-1500 CVC* manufactured by *XINGTONGLI*, each allegedly capable of supplying a direct output current of up to 1500 A and a voltage of up to 12 V, were purchased. Further, a dummy resistor represented by sheets of copper without an additional load (essentially a short-circuit setup) was constructed to simulate the electronic properties expected from the resonator coils.

When connecting the SMPS and the resistor together with A. Pelczar in the test setup shown in FIG. 5.4a, however, it could be established that the device did not in fact deliver a constant current as described by the manufacturer. On the contrary, it delivered pulses with current periods of 24.4 µs and dead time between 21.5 µs at 100 A decreasing to 7.4 µs at 760 A. The voltage curve for the latter can be seen in FIG. 5.4b.

This meant that the SMPS at it is cannot be used to supply MONOPOL. To fix the issue, the idea of inserting a smoothing capacitor was introduced. Therefore simulations with *LTSpice XVII* were performed. Since no commercially available capacitors can handle such high currents in a reasonable manner, it was calculated that an array of 380 capacitors with a capacitance of 680 µF each (Low ESR Electrolytic Capacitor, FR Series, 35 V, EEUFR1V681L) would provide a total capacitance of 0.258 F. The simulation proved successful and can be seen in FIG. 5.5.

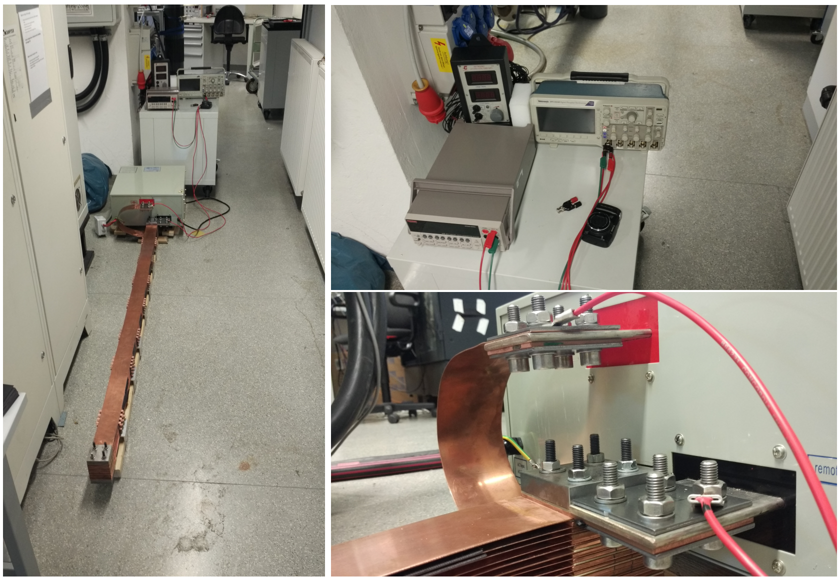

(a) Setup for the testing with the copper dummy resistor in the front connected to the SMPS (left), the used measurement instruments (top right), and the precise connection point arrangement (bottom right).

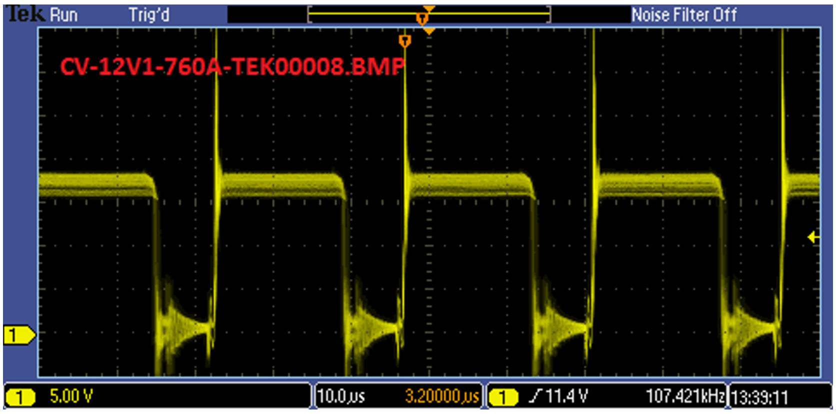

(b) Voltage curve of the SMPS at 760 A. Current periods of 24.4 µs are followed by a dead time of 7.4 µs. The transitions show quite long stabilising periods with overshooting voltage peaks of a factor two for the transition to from off to on.

FIG. 5.4 – SMPS testing setup with results.

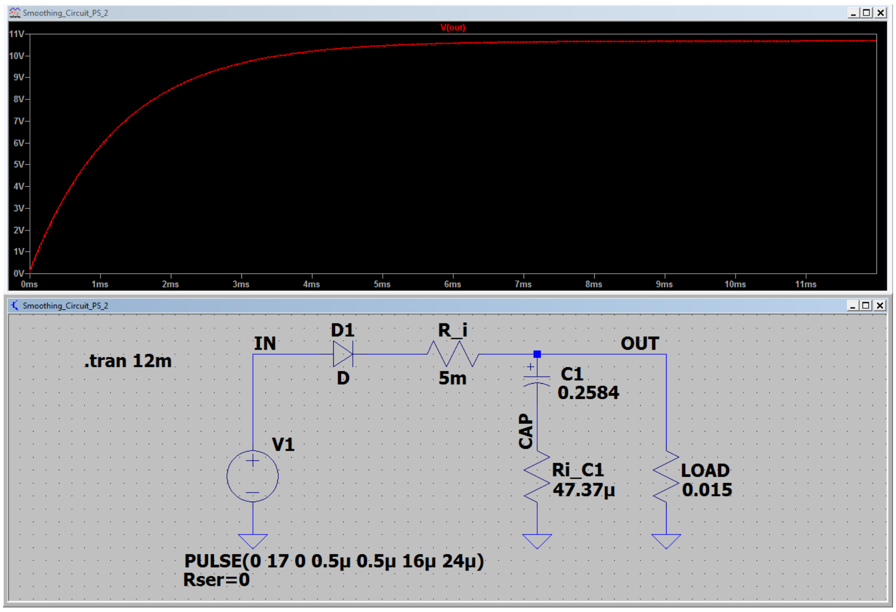

```
.tran 12m
PULSE(0 17 0 0.5µ 0.5µ 16µ 24µ)
Rser=0
```

FIG. 5.5 – Simulation of the smoothing circuit. A pulsed power supply V1 in combination with a diode D1 and a large R_i 5 MΩ resistor simulating the SMPS. The CAP arm of the diagram consists of C1, the array of 380 capacitors with a total value of 0.258 F, and an internal resistance of 47.37 µΩ. The OUT branch includes the load and represents the MONOPOL resonator with an internal resistance of 15 mΩ. The graph on top indicates the simulation of the voltage for the load and shows that the increase of voltage to a stable value of 10.5 V can be achieved in about 7 ms.

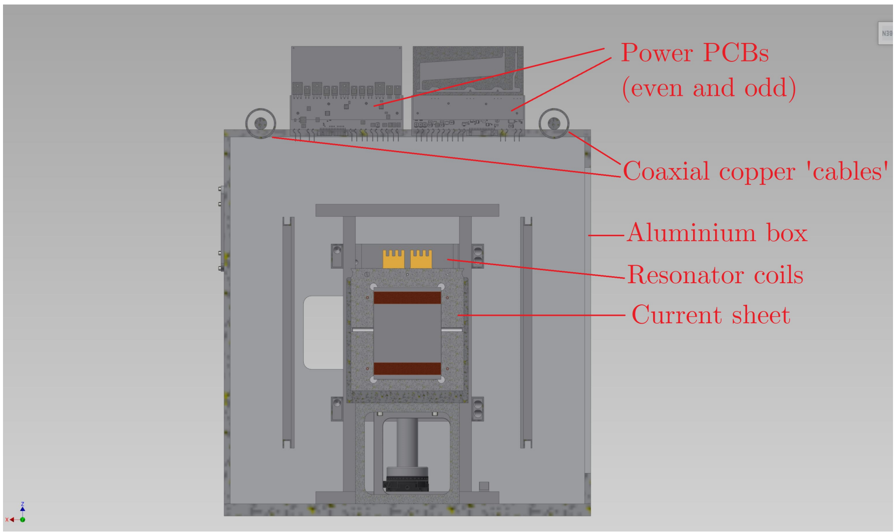

FIG. 5.6 – Technical drawing by R. Gergen of the front view of MONOPOL with the power supplies placed above the resonator.

5.4 Other novelties concerning MONOPOL

Regular MONOPOL group meetings were established together with E. Jericha, A. Frank, R. Gergen and A. Pelczar to discuss next steps in the work process arising problems concerning the construction of the resonator. It was decided that the new power supplies will be mounted above the resonator to prevent the strong currents of the resonator to interfere with the magnetic fields in the resonator. Two coaxial 'cables' consisting of a copper pipe and rod each will be utilised to guide the current from the SMPS to the coil power supplies and will be placed on the outside of the two racks of PCBs (odd elements on one side, even elements on the other) to keep the connecting cables as short as possible. A first technical drawing can be seen in FIG. 5.6.

Additionally, a copper box for the control board, which will be placed above the power PCBs, will be designed to ensure proper electromagnetic shielding of the highly sensitive components.

6 Conclusion and Outlook

The aim of this thesis was to improve the understanding of the thermal white beam and the specific spectrum measured at the TRIGA reactor of the Atominstitut by conducting polarised neutron experiments in preparation for MONOPOL 4.0.

The full functionality of the supermirrors as well as their spectral influences could be demonstrated and their degree of polarisation calculated with reasonable uncertainty and are expected to lie between 0.85 and 1.00. The two polarisers will take an important role in the future setup of the resonator and their intricacies should therefore be understood quite well to ensure the success of the experiment and the highest polarisation possible.

In addition, the efficiencies of the current-sheet and the DC-coil flippers in the thermal neutron range could be determined. While the DC-coil flippers will be replaced by the resonator, the broad-band flipper, the current-sheet, will be a permanent component of MONOPOL and its functionality and behaviour in the white beam is essential for the setup.

It could be shown how the different spin manipulation devices such as a current-sheet and DC-coil flippers influence the polarised neutron spectrum and that it is indeed possible, as had been planned, to use the MONOPOL resonator at the 'Thermal White Beam Facility' (TWB).

Since the entire electronic components were redesigned for MONOPOL 4.0, this brought some major changes in the setup with them as electromagnetic shielding of sensitive components and water-cooling were now necessary in order to ensure a successful and safe operation of the resonator. The successful testing of the main controller board and the initial operation of the backplanes with some of the individual power supply PCBs indicated that the designed electronic components are operational, communication can be established and are ready for testing with small loads.

The assembly and soldering of the cooling bodies and subsequent testing for leakage have also demonstrated that every single one is ready for use.

The experiments have also indicated that some of the improvements are still needed before finally putting the resonator in operation at the TWB.

Firstly, more detailed measurements for different angles could be of use to understand at which angles the polarisation degree is actually the highest. To perfect this, however, will take far more time due to the many degrees of freedom of the setup. It would be a major advantage to be able to remotely manipulate the linear stages of the supermirrors since this would enable an automation of multiple measurements for different positions. Upgrading the current programme used for the TOF measurements could aid in the automation process. This was not yet possible due to compatibility reasons for different versions of Labview.

Secondly, the compensation field for the current-sheet should be redesigned completely. Since it was not built in a Helmholtz-configuration, the compensation causes more problems than it solves. The currents for which it was designed are also not suitable for a white beam with a maximum around 1.8 Å due to the heat-up of the coils, especially because a reasonable guide field strength should easily be compensated. The resonance wavelength for Monopol depends on the guide field B_0 and to flip neutrons of 1.8 Å, a field of 3.09 mT is needed, and thus has to be compensated by a compensation field of equal magnitude. A suggestion would be to add cooling pipes for the compensation coil since a cooling system for the resonator will be in place in any case and could easily be modified to supply an additional device.

Thirdly, as shown in the previous experiments, the spin flip probability for the neutrons is quite wavelength-dependent when using the current-sheet. When only placing the CS between the supermirrors, changing the setup by turning it 90° around the neutron flight axis would omit the adiabatic rotation of the neutron spin before and after the transmission through the current-sheet (provided the CSs magnetic field points into the proper direction). This would eliminate the effects caused by the adiabatic process and permit to measure a 'dark field' directly indicating the number of neutrons that are not fully inverted when traversing the spin flipper. Such experiments would provide more insight into the efficiency of the current-sheet.

Fourthly, exact measurements of the magnetic field strength and local gradients within the guide field are only possible within certain constraints and with a limited accuracy. The magnetic field matrix consisting of an array of magnetic sensors and intended for a good spatial resolution has been designed by A. Pelczar and is currently under construction. The device will provide a simple and efficient way to measure the field distributions in the experimental setup.

Lastly, the next important step in the development of Monopol is the mount for the 48 individual PCBs with the heavy cooling bodies attached to them. It is of great importance that, since the PCBs will be placed on the fragile backplanes from above, the suspension is stable and keeps the components in place without damaging the connectors. As soon as the mount is available the testing phase for the resonator at the TWB can be initiated.

The MONOPOL project will be ready for initial testing at the white beam of the Atominstitut in the foreseeable future. As it is a complex experiment meticulous planning of each step is of the essence since errors could easily lead to damage and safety issues. However, the motto in such matters always is: One step at a time.

Bibliography

[1] CODATA Recommended Values of the Fundamental Physical Constants. `http://dlmf.nist.gov/`, Release 1.0.20 of 15/09/2018. F. W. J. Olver, A. B. Olde Daalhuis, D. W. Lozier, B. I. Schneider, R. F. Boisvert, C. W. Clark, B. R. Miller and B. V. Saunders, eds.

[2] G. M. Drabkin. Sov. Phys. JETP **16** (1963) 282.

[3] G. M. Drabkin, V. A. Trunov and V. V. Runov. Static Magnetic Field Analysis of a Polarized Neutron Spectrum. Sov. Phys. JETP **27** (1968) 194–196.

[4] G. Badurek, A. Kollmar, A. Seeger and W. Schalt. Use of a Drabkin spin resonator in inverted geometry neutron time-of-flight. Nucl. Instrum. Methods Phys. Res. A **309** (1991) 275–283.

[5] G. Badurek and E. Jericha. Upon the versatility of spatial neutron magnetic spin resonance. Physica B **335** (2003) 215–218.

[6] C. Gösselsberger. Entwicklung eines Wanderwellen-Neutronenspinresonators. Doctoral thesis, TU Wien, 2012.

[7] S. Gumpenberger. Implementation of a Spactial Magnetic Spin Resonator for Neutron Spectroscopy Applications. Diploma thesis, TU Wien, 2012.

[8] T. Gerstmayr. Ein magnetischer Wanderwellenresonator zur zeitlichen und spektralen Präparation polarisierter Neutronen. Diploma thesis, TU Wien, 2013.

[9] R. Raab. Weiterentwicklung eines Wanderwellen-Neutronenspinresonators für sehr kalte Neutronen. Diploma thesis, TU Wien, 2014.

[10] B. Berger. Experimentelle Umsetzung der Geschwindigkeitsselektion mittels Spinresonanz für sehr kalte Neutronen (VCN). Diploma thesis, TU Wien, 2013.

[11] J. Bosina. Charakterisierung eines 'Badurek'-Resonators für sehr kalte Neutronen. Diploma thesis, TU Wien, 2015.

[12] W. Mach. Installation of a neutron beam instrument at the TRIGA reactor in Vienna. Doctoral thesis, TU Wien, 2018.

[13] A. Frank. Konzept und Test einer Steuerung für einen magnetischen Wanderwellenresonator zur Wellenlängenselektion von langsamen Neutronen. Diploma thesis, TU Wien, 2018.

[14] M. Sajatovic. Parametrization Software for a Badurek Travelling Wave Mode Resonator. Project thesis, TU Wien, 2018.

[15] M. Wess. Controlling Software for a Badurek Travelling Wave Mode Resonator. Project thesis, TU Wien, 2018.

[16] J. Chadwick. Possible Existence of a Neutron. Nature **129** (1932) 312.

[17] W. G. Williams. Polarized neutrons. Oxford series on neutron scattering in condensed matter. Oxford University Press, Oxford, 1988.

[18] K. A. Olive and Particle Data Group. Review of Particle Physics. Chin. Phys. C **38** (2014) 090001.

[19] G. Badurek. The magnetic moment of the neutron. Lecture notes, TU Wien, 2016.

[20] K. H. Beckurts, K. Wirtz and L. Dresner. Neutron Physics. Springer, Berlin/Heidelberg, 1964.

[21] J. Byrne. Neutrons, Nuclei, and Matter: An Exploration of the Physics of Slow Neutrons. Institute of Physics Pub., 1994.

[22] D. Filges and F. Goldenbaum. Handbook of Spallation Research: Theory, Experiments and Applications. Wiley-VCH Verlag GmbH & Co. KGaA, 2009.

[23] A. Didi, A. Dadouch, M. Bencheikh and O. Jai. Monte Carlo Simulation of Thermal Neutron Flux of Americium–Beryllium Source Used in Neutron Activation Analysis. Moscow Univ. Phys. Bulletin **72** (2017) 460–464.

[24] M. F. James. Energy released in fission. J. Nucl. Energy **23** (1969) 517–536.

[25] Atominstitut der TU Wien. `https://ati.tuwien.ac.at/reactor`. Accessed on: 19/07/2018.

[26] Institut Laue-Langevin. `https://ill.eu/`. Accessed on: 26/07/2018.

[27] European Research Infrastructure Consortium. `https://europeanspallationsource.se`. Accessed on: 26/07/2018.

[28] F. Bloch. On the Magnetic Scattering of Neutrons. Phys. Rev. **50** (1936) 259–260.

[29] J. Schwinger. On the Spin of the Neutron. Phys. Rev. **52** (1937) 1250–1250.

[30] G. Badurek. Polarized Neutrons. Lecture Scripts of the 7th European Winter School on Neutrons and Synchrotron Radiation, 2011.

[31] Neutron Optics and Polarization. Lecture notes, University of Michigan, 2009.

[32] D. J. Hughes and M. T. Burgy. Reflection of Neutrons from Magnetized Mirrors. Phys. Rev. **81** (1951) 498–506.

[33] R. Pynn. Polarized Neutrons. Lecture notes, Indiana University Bloomington, 2006.

[34] F. Mezei. Novel Polarized Neutron Devices: Supermirror and Spin Component Amplifier. Communications on Physics **1** (1976) 81–85.

[35] T. Wilpert and C. Schulz. Helmholtz Zentrum Berlin, 2016. `https:/helmholtz-berlin.de/mediathek/info/material/neutronen/neutronenleiter-spiegel_en.html`. Accessed on: 03/08/2018.

[36] L. W. Alvarez and F. Bloch. A Quantitative Determination of the Neutron Moment in Absolute Nuclear Magnetons. Phys. Rev. **57** (1940) 111–122.

[37] F. Mezei. Neutron spin echo: A New Concept in Polarized Thermal Neutron Techniques. Z. Phys A **255** (1972) 146–160.

[38] E. Fermi, J. Marshall and L. Marshall. A Thermal Neutron Velocity Selector and Its Application to the Measurement of the Cross Section of Boron. Phys. Rev. **72** (1947) 193–196.

[39] G. F. Knoll. Radiation Detection and Measurement. John Wiley & Sons Inc., New York/Chichester/Weinheim/Brisbane/Toronto/Singapore, 2000.

[40] S. F. Mughabghab. Atlas of Neutron Resonances: Resonance Parameters and Thermal Cross Sections. Elsevier Science, 2006.

[41] C. Gösselsberger, H. Abele, G. Badurek, E. Jericha, S. Nowak, G. Wautischer and A. Welzl. Design of a Novel Pulsed Spin Resonator for the Beta-Decay Experiment PERC. Phys. Procedia **17** (2011) 62–68.

[42] M. M. Agamalyan, J. Schweizer, Y. M. Otchik and V. Khavronin. Optimization of the Drabkin Monochromator. Nucl. Instrum. Methods **158** (1979) 395–397.

[43] M. M. Agamalyan, G. M. Drabkin and V. I. Sbitnev. Spatial spin resonance of polarized neutrons. A tunable slow neutron filter. Phys. Rep. **168** (1988) 265-303.

[44] W. Mach, E. Jericha, M. Bacak, D. Hainz, A. Musilek, M. Villa and H. Abele. Installation of a Thermal White Neutron Beam Facility at the TRIGA Reactor in Vienna. Conference Proceedings of the 26th International Conference Nuclear Energy for New Europe (NENE) **502** (2017)

[45] E. H. Hall. On a New Action of the Magnet on Electric Currents. Am. J. Math. **2** (1879) 287–292.

[46] W. Demtröder. Experimentalphysik 2. Springer, Berlin/Heidelberg, 2017.

[47] R. Raab. Ausgewählte Experimente mit polarisierten Neutronen und Vergleich Messung zu Simulation. Project thesis, TU Wien, 2011.

[48] I. Hughes and T. Hase. Measurements and their Uncertainties: A practical guide to modern error analysis. Oxford University Press, Oxford, 2010.

[49] E. Jericha. Private communication, 2019.

[50] A. Danner. Private communication, 2018.

[51] A. Frank. Software-Entwicklung und Test der Steuerungselektronik für den Neutronenresonator MONOPOL. Bachelor thesis, TU Wien, 2015.

[52] A. Frank. Test der Steuerungselektronik für den Neutronenresonator MONOPOL. Project thesis, TU Wien, 2017.

List of Figures

List of Tables